SENSITIVITY OF THE OCEAN'S MERIDIONAL OVERTURNING CIRCULATION TO SURFACE CONDITIONS IN THE PALEOGENE

A Thesis

by

BRIAN ANDREW HAINES

Submitted to the Office of Graduate Studies of
Texas A&M University
in partial fulfillment of the requirements for the degree of

MASTER OF SCIENCE

August 2012

Major Subject: Atmospheric Sciences

Sensitivity of the Ocean's Meridional Overturning Circulation

to Surface Conditions in the Paleogene

SENSITIVITY OF THE OCEAN'S MERIDIONAL OVERTURNING CIRCULATION TO SURFACE CONDITIONS IN THE PALEOGENE

A Thesis

by

BRIAN ANDREW HAINES

Submitted to the Office of Graduate Studies of
Texas A&M University
in partial fulfillment of the requirements for the degree of

MASTER OF SCIENCE

Approved by:

Chair of Committee,	Robert L. Korty
Committee Members,	Gerald R. North
	Deborah J. Thomas
Head of Department,	Kenneth P. Bowman

August 2012

Major Subject: Atmospheric Sciences

ABSTRACT

Sensitivity of the Ocean's Meridional Overturning Circulation
to Surface Conditions in the Paleogene. (August 2012)

Brian Andrew Haines, B.S., Texas A&M University
Chair of Advisory Committee: Dr. Robert L. Korty

Deep circulations in the ocean affect the distribution of physical, chemical, and biological properties, and are intimately entwined with the planetary-scale climate. Numerous proxies, including neodymium (Nd) in fossil fish teeth, point to a source region in the South Pacific for much of the low-latitude deep-water during the early Paleogene. We use the MIT general circulation model (MITgcm) to test the sensitivity of deep-water formation to uncertainty in surface boundary conditions in a number of numerical modeling experiments with realistic and idealized bathymetries. Finally, the MITgcm is run with a passive tracer, ε_{Nd}, for some of the experiments mentioned above and to multiple initial surface distributions of ε_{Nd}.

In our experiments that use idealized basin shapes, appropriate for the early Cenozoic, the formation of North Pacific deep-water occurred in all of our experiments in which we vary the magnitude of the surface density gradient. While the rate of deep-water formation is sensitive to the strength of the surface density gradient, the location of the source regions was not.

For our experiments that use realistic bathymetry, the formation of South Pacific deep-water occurred in a majority of our experiments. Here the Southern Ocean has the greatest poleward latitudinal extent, and therefore preference for deep-water formation. When salinity is added into the equation of state we find that this causes an increase in the extent of Southern Ocean deep-water.

Lastly, we explore simulations using ε_{Nd} as a passive tracer. Throughout most of the realistic simulations explored, the densest water occurs in the Southern Ocean. There is a strong sensitivity to where in the Southern Ocean the densest water occurs though, either in the South Pacific or Atlantic. With ε_{Nd} values different in these regions, various simulations produced different tracer distributions. We found this variability in the sinking region to be very sensitive to runoff and seasonality. The sensitivity to the spatial distribution of surface and interior ε_{Nd} values was found to have little affect on the final ε_{Nd} distribution, given that the ε_{Nd} value in the sinking regions was kept constant.

DEDICATION

To my loving wife

ACKNOWLEDGEMENTS

I would like to thank my committee chair, Dr. Korty, and my committee members, Dr. North, Dr. Thomas, and Dr. Lyle, for their guidance and support throughout the course of this research. I am forever grateful to my advisor, Dr. Robert Korty, whose unwavering confidence in me always inspired me to me more than I was. It was truly a blessing to work with such a talented individual.

During my study at Texas A&M I was fortunate enough to spend a week at Purdue University. While there Dr. Matthew Huber, one of our group's collaborators, helped me tremendously to develop new possible avenues for my research. He challenged me to look at things from a different perspective. I'm extremely thankful for his help throughout my research project.

Thanks also to my friends and colleagues and the department faculty and staff for making my time at Texas A&M University a great experience. I also want to extend my gratitude to the National Science Foundation, which helped make this study possible.

Finally, thanks to my mother and father for their encouragement and to my wife for her patience and love. There were countless nights that I would come home and talk about my research and new possibilities to her. Each time she would listen meticulously and offer her unfailing love and support. I am forever grateful.

TABLE OF CONTENTS

LIST OF FIGURES

FIGURE Page

LIST OF TABLES

1. INTRODUCTION

In the present climate, water sinks in the North Atlantic and Southern Ocean where it is densest. The locations of deep-water formation were not always the same though, as differences in surface temperatures, winds, precipitation, and continental positions over geologic time scales affected the surface density field. During the early Cenozoic (65 to ~50 million years ago [Ma]) southern high latitude annual-mean sea surface temperatures (SSTs) were at least 10°C (Stott et al., 1990; Zachos et al., 1994 and Bijl et al., 2009), while Arctic SSTs have been estimated to be as high as 15- 18°C (Sluijs et al., 2006). Tropical SSTs during the period were warmer than today, with estimates ranging from 28 -32°C (Pearson et al., 2001) to as high as 35-40°C (see, e.g., discussion in Huber 2008). Estimates of bottom water temperatures show they too were substantially higher, about 8 - 12°C (Zachos et al., 2001), than deep-sea temperatures of today. Given the very different and much warmer surface climate during these times, the regions of deep-water formation may also have been different than today.

Over the last quarter century, two distinct hypotheses emerged to explain the warm bottom waters common during the early Cenozoic. One posited that low latitude waters, which though warm could also have been dense because of high salinity, sank in the Tethys Sea (Barron and Peterson 1991; Wright and Miller 1993). But later refinements to estimates of surface temperatures, model simulations, and analysis of deep-water chemical tracers have lended increasing credence to an alternate view that deep-waters

---

This thesis follows the style of *Journal of Paleoceanography*.

formed at high latitudes in the Pacific (Thomas et al., 2008; Nunes and Norris, 2006; Thomas, 2005; Wright and Miller, 1993).

Thomas (2005; 2008) used neodymium (Nd) isotope ratios, ε_{Nd}[1], to characterize the deep-water source region. She found the signature of abyssal water in various drilling sites located around the equatorial Pacific (e.g., Figure 1). Nd has a long enough residence time so that water retains the signal it was first "assigned" at the surface as it moves around the ocean interior. The Nd acts like a tag for where the deep-water originated. If the residence time was shorter, the water would lose its tag before it had a chance to move about the ocean basin. Yet Nd has a residence time that is shorter than that of the deep-water circulation; if Nd had a residence time longer than that of the abyssal circulation, the intial signal would be lost in other parts of the ocean basin, as the old signal would be contaminated with new Nd surface values. Therefore, the residence time of Nd make it ideally suited as a water mass tracer. Nd enters the oceans through continental weathering and runoff of exposed rocks (Jones et al., 1994; Goldstein and Jacobsen, 1988; Elderfield and Greaves, 1982; Halliday et al., 1992). The most negative, or most non- radiogenic, ε_{Nd} values come from older continental rocks. Greater ε_{Nd} values are more radiogenic, and come from newer rocks[2].

During the late Cretaceous (70 Ma) ε_{Nd} values were most radiogenic in the North Pacific, with relatively non-radiogenic values occurring in the Atlantic, Indian and Southern Oceans. Core and crust data from the equatorial Pacific exhibited relatively

---

[1] ε_{Nd} is the ratio of Nd isotopes (^{143}Nd to ^{144}Nd) commonly used to measure the departure from a normal ratio

[2] In today's world, the most radiogenic ε_{Nd} values come from areas of the North Pacific, $\varepsilon_{Nd} \sim -4$, were volcanism is occurring, i.e: newer rocks being made. The most negative values come from the North Atlantic were runoff comes from old Canadian rock, $\varepsilon_{Nd} \sim -12$.

unradiogenic ε_{Nd} values, which indicate an influence of a Southern Water Mass (Thomas, 2005; 2008). By the start of the Eocene (~55 Ma), deep-water influence had shifted towards the Northern latitudes of the Pacific, or relatively more radiogenic ε_{Nd} values (Thomas, 2005 ; 2008). At 35 Ma the ε_{Nd} signal had shifted to a relatively non-radiogenic value again. The sensitivity of surface conditions and interior ocean properties that might cause this change of deep-water influence is something this study is trying to capture.

Our present goal is to analyze how processes and conditions in the early Cenozoic climate established deep-water formation locations, and how sensitive they are to the uncertainty inherent to estimates from proxies. From the work stated above, this study hopes to ascertain what could cause a shift in influence of deep- water production. In particular, what ranges of various surface and interior ocean variables could produce a dominant deep-water signature in different areas of the ocean, such as the North Pacific or Antarctic? What could cause a sudden shift of deep-water production? Is there a reasonable range of variables that supports the findings above?

Although there is increasing model-based and proxy-derived evidence that waters sank in high latitudes of the Pacific, the sensitivity of deep-water formation to slight changes in surface conditions and interior properties of the ocean has not been explored. Many of the specific values for these quantities are unknown or are not well enough constrained to precisely stipulate, and so our primary goal will be to understand what effects this uncertainty has on simulations of deep-water circulations during this period.

2. BACKGROUND

Initial reconstructions of early Cenozoic climate overestimated the weakness of the meridional temperature gradient during the Eocene, as temperature in the tropical surface ocean waters were believed to be colder; error in these estimates came from underestimating the extent of diagenesis in buried sediment, (e.g., Schrag, 1999). The idea of planet earth having such a weak temperature gradient, gave rise to the concept of an "Equable Climate", and it posed several immediate problems. How could such a weak temperature gradient be sustained, given that the baroclinic wave responsible for transporting much of the heat poleward themselves depend on meridional temperature gradients? Why were surface waters of the tropics cooler in the Eocene than present day?

Barron (1987) attempted to explain how this weak gradient could be maintained by performing the first modeling studies of these ancient periods. The eolian sediments of the time indicated a weak atmospheric circulation and high seasonal continental climates indicative of a weak temperature gradient. Paleobotanical evidence pointed to a more mild seasonality though. This inconsistency led Barron to be cautious about interpreting the data. Could the ocean have played a bigger role in redistributing heat? This question lead to later experiments testing the magnitude of the meridional overturning circulation (MOC) during the Eocene to determine if this redistribution of heat was possible by the ocean. In an effort to try and explain this weak temperature gradient, a hypothesis arose that deep-waters could have possibly formed from a subtropical source during the

Eocene (Barron and Peterson, 1991). This hypothesis postulated that because the oceans around the globe were similar in temperature, the saltiest parts would therefore be densest. The densest areas would occur where there was greater evaporation than precipitation, i.e. the subtropics. One area in particular where sinking was thought to occur was the Tethys Sea. Work continued on for a couple more years supporting warm deep saline water (WDSW) formation in the Tethys Sea (Wright and Miller 1993). Wright and Miller looked at some evidence from calcite that could reflect the presence of WSDW below colder fresh water. Marotzke (1989) used a single hemisphere model and found solutions in which deep-water production oscillated between high latitudes and the subtropics, but only when no wind forcing was used. Later, Weaver et al. (1991) found sinking modes that oscillate between high and low latitudes when freshwater flux is increased in the presence of wind forcing only.

More recent work has identified the source of deep-water formation most likely to be polar regions (Thomas, 2005 and 2008; Nunes and Norris, 2006). Thomas used Nd isotopic data stored in fossil fish teeth to show that deep-water formation most likely occurred in the polar regions in a bimodal type of production. Later model runs (Huber and Sloan, 2001; Bice and Marotzke, 2001) also support the view of sinking occurring at high latitudes. The question of whether sinking occurred at high northern or high southern latitudes or both is also important to understand. Bice and Marotzke (2002) attempted to answer this by using an ocean model with mixed surface forcings. Sensitivity tests were performed on varying paleoceanographies, in which a switch in deep-water production was caused by a slow increase of the atmospheric hydrologic cycle (increasing evaporation in the subtropics and higher net precipitation at higher latitudes). Then the same model configuration was used except the configurations of the continents were altered. This different configuration influenced whether or not deep-water production switched from northern to southern high latitudes.

Further work has also been done on how different geometric configurations affect the MOC (Von der Heydt and Dijkstra ,2006; 2008). Von der Heydt and Dijkstra in 2008 had four different continental geometries. These different geometries included: a symmetric case with the Atlantic and Pacific Oceans being equal in size, an asymmetric geometry with the Pacific basin being taller than the Atlantic basin, and also a asymmetric geometry with a Tethys gateway. The model was run with different perturbations of surface salt flux.

There has also been work on using different types of boundary conditions for ocean general circulation models (OGCMs). Even though fully coupled models offer the advantage of full interaction, historically they have required flux adjustments to produce present day climate. Also their computational expense is high. For this reason OGCMs can be used. The question arises though, how should the boundary conditions be applied to the model? The most common OGCM boundary condition is to restore the surface values to a certain value, e.g., climatology, with a certain e-folding time (e.g., Cox and Bryan 1984; Danabasoglu and McWilliams 1995). The issue with restoring the boundary conditions is that is neglects the possibility of having nonzero fluxes occurring with correct model surface fields, i.e., could the given SST field come from the same evaporation and precipitation fields as the salinity field does? The chance of the fluxes being zero throughout the entire integration is slim. A better boundary condition is to derive the salinity field from the evaporation and precipitation fields and restore the SST field, e.g., use mixed boundary conditions (see Tziperman et al., 1994). Still, the problem is that the evaporation and precipitation fields have been prescribed, i.e., a lack of air-sea interaction.

There has been work done using bulk forcing boundary conditions instead of restoring or mixed boundary conditions (Large et al., 1997). It has been shown that bulk forcing boundary conditions produce poleward heat and salt transports that better agree with oceanographic estimates. This is not suprising since bulk forcing allows the atmosphere to “interact” with the ocean. This is accomplieshed by providing the OGCM with a precipitation, a solar flux, longwave flux, air temperature and humidity files. Therefore the SST is calculated as a function of the solar and longwave flux data. Also from the flux files evaporation can be calculated which can then intern calculate the sea surface salinity. Bulk forcing therefore allows for a better estimate of the boundary conditions given the air-sea interaction.

3. MODEL INFORMATION

For this study, we use the MIT General Circulation Model (MITgcm) (Marshall et al., 1997a; Marshall, 1997b), which is a full physics model that solves the incompressible Boussinesq primitive equations. The model is run as an ocean only model in hydrostatic balance. We used various bathymetry files, which can be broadly partioned into idealized and realistic categories.

The MITgcm model was forced with various wind and temperature profiles. In the case of the intial idealized runs (see section 4), a wind profile (e.g., Figure 2) was derived from a modern annual mean zonal wind (Hellerman and Rosenstein, 1983) invariant in time. The profile is nearly symmetric about the equator, but the peak in the Southeren Hemisphere is shifted southward to better fit the location of the Drake Passage. The temperature profile intially prescribed (e.g., Figure 3) was choosen so that the density gradient mirrors that observed in present climate (e.g., Peixoto and Oort, 1992, p. 193). This was changed in subsequent model runs to determine the sensitivity of the imposed gradient.

The time step varied between 1440 and 7200 steps per year for model runs, and was chosen to ensure numeric stability. Each model was run to equilibrium (~3500 years), and diagnostics were computed from data avereaged over the final century.

One final note, in the figures we present here, we do not include Bolus velocities. Once added back into the Eulerian mean velocity (Gent et al., 1995), much of the Deacon cell in the southeren hemisphere disappears.

4. IDEALIZED BATHYMETRY

Compared to deeper geologic time, the continental positions are broadly similar to the present-day map, but there are several important differences that can affect ocean circulations and water mass distributions; figure 4 shows a map of the early Cenozoic. The Atlantic Ocean is narrower and does not extend as far north compared to present day, while the Pacific Ocean is wider and extends farther north. A shallow opening around present day Panama separates the two oceans, with no deep-water passage occurring between the two oceans. The Drake Passage is estimated to have opened approximately 34- 30 Ma (Livermore et al., 2005), which then allowed for the Antarctic Circumpolar Current to develop corresponding closely to the glaciation of Antarctica.

For the geography of the early Cenozoic, we explored sensitivity to changes in surface boundary condition including the shape and location of continental barriers, surface meridional temperature gradients, and surface wind profiles. For the results in this section, we imposed a surface density gradient to which values are restored over a 30-day relaxation period. To accomplish this, we turned off salt advection and simplified the model's equation of state so that the temperature alone determines the density.

$$\rho = \rho_0\left(1-\alpha T\right) \tag{1}$$

With this simplification, supplying the model with a temperature of 0 ˚C yields the reference density, ρ_0, of 1027 kg m^{-3}. We use this formulation for the idealized experiments reported in this section. For most of the more realistic simulations discussed in later sections, we use the full equation of state and allow temperature and salinity to evolve independently. We have tested a variety of different configurations using idealized geography in the MITgcm to examine the effects of open or closed passageways in Central America, the Tethys Sea, and the Drake Passage (a full list of parameters used in the idealized section can be found in table 1).

4.1 Effects of open passageways

We ran an experiment with idealized topography corresponding to the continental distribution in today's world, as shown in Figure 5. The principal features include a wide ocean that corresponds to the Indo-Pacific basin separated from a narrower basin extending further north (i.e., the Atlantic) by two passageways in the Southern Hemisphere: a full-depth opening south of 30 ˚S representing the waters south of Africa and a Drake Passage with a ~3000 meter deep sill.

The MOC for this case is plotted in Figure 6. It captures the salient features of the modern ocean circulation: sinking in the North Atlantic and Southern Ocean with a return of dense, deep-water parcels to the surface throughout the Pacific. (This is accomplished in major part by diapycnal mixing, whose sources of energy are the tides and surface winds.) The strength of the North Atlantic overturning circulation is sensitive to the value of the diapycnal diffusion coefficient (κ) as well as the structure of the surface density gradient. We explore these dependencies in further detail later, but for the simulations discussed in this subsection κ was set to 0.3 cm^2 s^{-1} and the surface temperature gradient entirely determines the density structure.

We explored how the prominent changes in the geography during the early Cenozoic affected the global circulation by testing a suite of similarly idealized continental distributions using the same surface conditions and mixing value. Figure 7 shows four different configurations. In Fig. 7a, the sole difference is that the wide Pacific-like basin extends further north than the narrower Atlantic; this is one of the major differences in early Cenozoic geography (see Fig. 4). Fig. 8 shows the overturning circulation for this case. By extending the Pacific further north and leaving a surface density function that depends only on latitude, the densest waters in the Northern Hemisphere are now located in the Pacific. The Atlantic has little circulation below the thermocline, though there is some weak upwelling of dense parcels by mixing.

But as noted earlier, the Drake Passage did not open until later in the Cenozoic (Livermore et al., 2005), so we tested the effects of a low latitude opening between the Atlantic and Pacific corresponding to the Central American Seaway (CAS). Its depth during this geologic interval is uncertain (Molnar, 2007), so we tested both a shallow opening and a deeper one at the same location, as depicted in Figs. 7b and 7c. With the closure of the Drake Passage, the intensity of the North Pacific circulation weakens in magnitude (to a maximum of 19 Sv), but the global structure is broadly similar to that shown in Fig. 8. The depth of the CAS had no effect on the strength or structure of the global overturning or large-scale ocean heat transport.

Finally, we tested the effects of an open Tethys Sea as shown in Fig. 7d. Figure 9 shows the MOC for this case, which has the most realistic early Cenozoic continental distribution of the idealized geography experiments. The low-latitude channel circumnavigating the globe has altered the overturning in the Pacific: the water that sinks in the north now upwells at low latitudes (similar to what happens in single hemisphere, single basin models; see, e.g., Weaver and Sarachik 1991). As a result, the North Pacific overturning cell appears more locally isolated than it did in the other geographic configurations.

In summary, when the Pacific extends further northward than the Atlantic Ocean, water sinks in the North Pacific because it is densest there. The CAS causes the sinking in the North Pacific to weaken compared to an open Drake Passage. The depth of the CAS had no effect on the structure of the circulation. The addition of the Tethys seaway did not affect the strength of the N. Pacific MOC but did affect its reach into the Southern Hemisphere.

4.2 Effects of temperature gradients

Next, we look at the effect of the temperature (density) gradient on the MOC using the idealized Cenozoic topography shown in Figure 7d. First, we examine how the magnitude of the temperature gradient affects the MOC; the various gradients tested are shown in Fig. 10. The control run temperature gradient (ΔT[3]: 25°C) is plotted in blue and is slightly asymmetric about the equator: the northern most point grid point for the

---

[3] ΔT is temperature difference between the equator and pole

ocean is 72°N while the southern most point is at 68°S, both of which are set to have the same minimum temperature. This is the same control temperature gradient used for all of the simulations reported in Section 4a. We tested two modifications to this control gradient: one stronger and one weaker gradient. The stronger gradient (ΔT: 39°C) is plotted in black, while the weaker gradient (ΔT: 12°C) is plotted in green. Finally, we look at how the sensitive the structure of bimodal sinking is to the degree of asymmetry in the meridional temperature gradient (Figure 11).

How does the size and rate of the overturning cell change from the control run, in Fig. 9, when the strength of the temperature gradient is altered? When the gradient is increased the strength of overturning increases in both the North Pacific and Southern Ocean, with a bit stronger increase in the Southern Ocean. The extent of both the overturning cells remains roughly the same compared to the control case. When the temperature gradient is reduced, the rate of overturning decreases in both deep-water formation locations. The key difference is that deep-water formed in the Southern Ocean now tends to upwell more in Atlantic Ocean. This allows for the deep-water formed in the North Pacific to flow through much of the North Pacific. The runs also qualitatively follow the scaling arguments of Welander (1971):

$$\Psi \sim \Delta T^{\left(\frac{1}{3}\right)} \tag{2}$$

although the exponential dependence is weaker here in these wind-driven circulations. As the temperature gradient increases, the strength of the overturning increases by a power to the third.

Lastly, we tested the sensitivity of the circulation to the degree of asymmetry in the temperature gradient, as depicted in Figure 11. As stated previously, the control run temperature gradient has quasi-equal overturning at both the North and South Pacific. We varied the Southern Hemisphere minimum temperature over a range from 4˚C cooler to 7˚C warmer than the lowest temperature in the north (-5˚C). As shown in Fig. 12, when the water is coldest in the Southern Hemisphere, the strength of the overturning cell that originates there is strong, while it greatly diminishes in the Northern Hemisphere. As expected, the reverse is true (i.e., when the Southern Ocean temperature is warmer than the North), the Northern Pacific cell is strong with nearly absent overturning in the South. When the minimum hemispheric temperatures are equal, there is sinking in both hemispheres, though it is strongest in the North (23 Sv compared to -15 Sv in the South).

In summary, the strength of the gradient does affect the MOC. The location of the coldest, densest, water is where the location of the strongest overturning will take place. As the temperature gradient is increased the strength of the MOC is increased and vice-versa. The asymmetry of the gradient also affects the location of deep-water. When the location of the coldest water is changed the deep-water formation region changes accordingly. As the temperature is constantly increased in the South Pacific the rate of overturning in the North Pacific increases until a certain point. Past a certain temperature increase in the South, the rate of increase in the North Pacific overturning stagnates.

4.3 Effects of wind stress

Next, we examined how changing the magnitude and position of the wind stress alters the MOC using the same idealized Cenozoic topography.

We tested the sensitivity of the MOC to different magnitudes of the wind stress, as shown in Fig. 13. The original wind stress profile (τ) is plotted in black with black circle markers, which is the wind stress profile used in all previous model runs discussed (i.e., the control run wind stress profile). We tested the sensitivity to doubling and halving the strength of the original profile. For the wind stress profile multiplied by two (blue line), the surface wind driven Ekman cells drastically increases in strength, and the northern overturning cell increases from 20 to 28 Sv. The overturning cell in the Southern Ocean remains about the same as in the control case. The extent of the southern deep-water is slightly reduced. When we halved the original wind stress profile (red line) the maximum rate of overturning edged down in both the North Pacific and Southern Oceans. The extent of deep-water return in the Pacific Ocean decreased, while it increased in the Atlantic Ocean.

We also tested the sensitivity of the position of the wind stress maxima in the ~50° absolute latitude region; the profiles can be found in Fig. 14. In each of the shifted profiles the wind stress maximum was shifted poleward by 4°. The shift to the south (red line) caused the mid-latitude wind driven cell to correspondingly shift southward and partly connect with the overturning circulation in the Southern Ocean. The rate of overturning for the cell has roughly remained the same, ~2 Sv decrease, and the extent of the cell has roughly stayed the same. The northern overturning circulation is about the same also. When the maximum wind stress is shifted northward (blue line), there is a slight decrease in the rate of southern overturning, again about 2 Sv, while rate of overturning in the northern cell is the same. The extent of both cells is similar to the test case.

In conclusion, the position of wind stress maxima has little effect on the rate of overturning, and the change in the extent of the cells is also minimal. There is a bigger impact on the size and extent of the surface driven wind cells, as expected. The strength of the wind stress does affect the rate and extent of the overturning cells. The stronger the wind stress, the rate of overturning generally increases, while the extent slightly decreases. When the wind stress weakens, the overturning decreases and its extent increases.

4.4 Effects of mixing

Lastly, we examine the effect of mixing on the MOC for the idealized Cenozoic topography. We tested the effects of several different mixing schemes, including different values for the diapycnal diffusivity, spatially varying dependencies, and transiently varying parameterizations. Here we highlight the effects of only one such experiment, using the classical depth dependent profile introduced by Bryan and Lewis (1979). The structure is shown in Fig. 15; we tested two distinct profiles that both increase to large abyssal values, but transition from lower near-surface values at different depths. We compare the changes to the same control case, whose circulation is shown in Fig. 9, which had a constant value of κ set to 0.3 cm^2s^{-1}. Both of our depth-varying profiles begin with the same value of κ (0.3 cm^2s^{-1}) near the surface, and transition to a stronger abyssal value of 1.5 cm^2s^{-1} abruptly.

When the transition to higher values occurs deep in the water column (e.g., 2000 m, as shown in Fig. 15b), the circulation is little different from the case with weak mixing throughout. The maximum of the overturning streamfunction in the North Pacific increases ~10%, but the structure is otherwise similar to that shown in Fig. 9.

When the transition to higher abyssal values occurs at a shallower depth in the thermocline (e.g., 600 m), there is a substantial response in both the North Pacific and Southern Ocean. The stronger overturning in the North Pacific, from 20 to 33 Sv, has created a curtain of sinking water that has made it difficult for deep-water from the Southern Ocean to slide below that of North Pacific origin. The result is deep-water that formed in the Southern Hemisphere now has a strong presence in the Atlantic but not in the Pacific Ocean.

Another set of runs with an identical setup, except using the topography seen in Fig.7c, was more extensively tested using the profile introduced by Bryan and Lewis (1979). A summary figure of the results can be found in Fig. 16. Fig. 16a/c illustrates the point that changing the mixing value in the thermocline has the greatest effect on the rate of overturning. Fig 16b/d also demonstrates that most of the heat transport in the ocean is done in the thermocline. As the thermoclines mixing value increases the maximum heat flux increase.

In summary, as the transition depth of weak to strong mixing becomes shallower the rate of overturning increases in both the North Pacific and Southern Ocean compared to the test case. Also, penetration of deep-water in the Pacific Ocean is reduced, while it is increased in the Atlantic Ocean.

5. REALISTIC BATHYMETRY

Figure 17 shows the realistic bathymetry used in the MITgcm for the early Cenozoic, which is taken from reconstructions of the late Eocene epoch by Matthew Huber (e.g., Huber et al., 2004). Our realistic bathymetry has a uniform 4˚ x 4˚ latitude-by-longitude grid. Comparing Figure 17 to 7d shows that in a broad sense the realistic bathymetry has similar characteristics compared to the idealized cases examined in the last section. The Pacific Ocean that is much bigger than the Atlantic Ocean, and there are openings in Central America and the Tethys Sea.

In the previous section, we investigated the sensitivity of the MOC to modifications in boundary conditions including open passageways, temperature profile, wind stress, and mixing. For this set of model runs, output from simulations of the National Center for Atmospheric Research (NCAR) Community Atmosphere Model version 3.1 (CAM3) was used (e.g., Huber and Caballero, 2011 and 2010). The simulations vary CO_2 by progressively doubling from the pre-industrial level of 280 ppm, to 560 ppm (one doubling), 1120 ppm (two doublings), 2240 ppm (three doublings), 4480 ppm (four doublings), and 8960 ppm (five doublings). The first four cases, 280 – 2240 ppm, were coupled to a slab ocean, with fixed ocean heat transport. The warmest cases (2240[4]- 8960 ppm) used constant sea surface temperatures (SST) taken from equilibrated coupled runs from the Community Climate System Model version 3 (Huber and Caballero, 2011 and 2010; Ali and Huber 2010; Liu et al., 2009;

---

[4] There were two cases for 2240ppm: one with and one without coupling

Hollis et al., 2009). The result of doubling CO_2 was an increase in the global mean temperature (see Fig. 18). The four slab ocean cases and the three constant SST simulations gave us a total of seven different sets of boundary conditions for temperature, wind stress, evaporation, and precipitation.

In the control run case for the various CO_2 levels, section 5a, the linear equation of state was again used (see, e.g., equation 1) with a 30- day restoring time period for the temperature. Salinity was not yet included in the control run (see section 5.1), but in all subsequent sections the full polynomial form of the equation of state for seawater is used (Jackett and McDougall, 1995). The salinity was calculated by subtracting CAM3 precipitation data from the evaporation data (E-P). The data was then normalized so that in one-year there is not net flux of water into or out of the ocean. Here we also now employ mixed boundary conditions (Large et al., 1997), allowing salinity and temperature to evolve independently.

5.1 Effects of varying CO_2

Figures 19 and 20 show the various overturning circulations in the Pacific Ocean for the slab and constant SST Ocean using the realistic Eocene bathymetry, not yet including salinity. For the 280 ppm case (E0), seen in Fig. 19a, there is overturning in both the North Pacific and Southern Ocean. The overturning in the Southern Ocean is dominant with deep-water seeping northward through the Pacific Ocean. In the 560 ppm case (E1), seen in Fig. 19b, there is again overturning in both the North and South with deep-water penetration far into the North Pacific. In Fig. 19c, 1120 ppm case (E2), the overall structure of the overturning is the same, but now the sinking in the Southern Ocean is dominant. In Fig. 20a, 2240 ppm case (E3), the trend continues, stronger overturning in the Southern Ocean with decreased sinking in the North. By this point the sinking in the North Pacific is almost non- existent. Fig. 20b is for the 2240 ppm case with data from the CAM3 model with a fixed ocean SST (E3k). Sinking in the North Pacific is still weak with a strong rate and extent of the overturning cell in the Southern Ocean. Fig. 20c illustrates the overturning for the 4480 ppm case with constant SST (E4k). Sinking in the Southern Ocean has remained roughly the same compare to E3k with sinking in the North Pacific nullified. The extent of sinking in Southern Ocean is still the dominant deep-water source reaching all the way into the North Pacific.

Comparing the MOC from the realistic bathymetry, Fig. 19a, to the MOC from the idealized bathymetry, Fig. 9b, shows that there are some similarities. There is sinking in both the North Pacific and Southern Ocean with a tongue of Southern Ocean deep-water cutting under the overturning cell in the North Pacific. The main difference is that the strength of overturning in the Southern Ocean is greater in the realistic bathymetry.

In summary, with higher concentrations of CO_2 the air warms causing a change in the spatial temperature distribution and gradient, Fig. 18. For E0 there is overturning occurring in both the Southern Ocean and North Pacific. The Southern Ocean overturning cell has a dominant presence in the Pacific Ocean. As the climate warms, overturning generally increases in the Southern Ocean and significantly weakens in the North Pacific.

5.2 Effects of salinity

Next we examine the effect of adding salinity, calculated from the E-P CAM3 data, to the MITgcm using mixed boundary conditions and the full polynomial form of the equation of state. We also look into the sensitivity of the MOC by modifying the amplitude of the evaporation minus precipitation. Figure 21 highlights the results from simulations, using the bathymetry in Fig. 17, in which salinity was and was not included (see section 5.1). Figure 22 shows the results in which the amplitude of E-P was increased and decreased.

Figure 21a displays the maximum rate of overturning in the North Pacific from model simulations in which CO_2 was linearly increased from 280 ppm to 5560 ppm. The trend that is apparent without salinity is the same when salt is included, except that the magnitude of the overturning is reduced with salt. When salt is added, the overturning circulation in the North Pacific almost completely vanishes. As the level of CO_2 increases the rate and extent of overturning in the North Pacific decreases. Figure 21b highlights the maximum rate of overturning in the Southern Ocean. The trend is the same whether or not salt is included; when the concentration of CO_2 increases, the rate of overturning increases until extreme levels of CO_2 are reached. The addition of salt itself causes a reduction in the rate of overturning. The extent of the Southern Ocean overturning cell remains roughly the same as the cases without salinity.

Next, we look at how the amplitude of E-P affects the MOC. The amplitude of E-P was altered by multiplying the evaporation and precipitation fields by a constant and then normalizing the data (see, equation 3).

$$\iint \left(a * (c * E) - (c * P)\right) (r^2 \cos(\varphi) d\lambda d\varphi) \tag{3}$$

In equation 3 r is the radius of the earth, a is the normalization constant, and c is the magnitude constant we used to alter the amplitude. The integral is summed up over the latitude (φ) and longitude (λ). We look at two different cases from the initial salt case discussed in the previous paragraph (see Fig. 21 salt included) that had a magnitude constant of 0.7. One case has a larger amplitude of E-P (c = 1), and another case has an amplitude that is smaller than the previous salt case (c = 0.4). Figure 22 highlights the results. The red triangles and green dots are the same as the ones plotted on Figure 21. The black stars indicate where the amplitude of E-P has been increased from the control run case, and the blue squares represent where the amplitude of E-P has been reduced from the control run case. The most apparent result is that when the amplitude of E-P is the greatest the Southern Ocean MOC is the lowest. This trend appears to also be true for the North Pacific, but since the MOC is weak to begin with, it is hard to see a clear signal. Also, the small E-P amplitude case usually has MOC values that fall between the case that included salt, normal E-P amplitude (green dots), and the no salt case or control run (red diamonds). From this graph it is easy to see a pattern. As the density dependence on salinity increases, the rate of overturning decreases in the Southern Ocean. The extent of the overturning also tends to decrease as the salinity dependence increases.

In summary, when salt is added into the model, the strength of overturning is lower than when the model was run without it. When CO_2 concentration is increased, the rate of overturning generally increases in the Southern Ocean and decreases in the North Pacific. This trend remains intact whether or not salt is included. When the amplitude of E-P is increased there is a further reduction in the rate of overturning.

5.3 Effects of runoff

Next, we inspect the effects of the magnitude and spatial distribution of runoff on the MOC. We test the effects by subtracting the runoff from the evaporation and precipitation data and then normalizing the field. In the previous realistic simulations, most revealed sinking occurring in the Southern Ocean. We felt it prudent then to add runoff in various places in the Southern Ocean to see how strong this sinking signal is. Could a slight influx of freshwater switch the location of deep-water formation?

Initially we started with runoff located in the South Pacific coming off of the Antarctic coast, see e.g, Fig. 23a. The E-P field including runoff is almost identical to the E-P field used with out runoff, except there is a slight difference due to the need to rebalance the field when runoff is included. The strength of the runoff was chosen by looking at the rate of discharge of today's rivers. The Mississippi river was chosen as a starting point since it has a high discharge, 16,200 $m^3 s^{-1}$ (Kammer, 1990), but is not unreasonably high. Next we divided by the area of the grid box we would like to spread the runoff over, i.e., drainage area, and we arrived at the runoff rate. Figure 24 shows the results with and without runoff included (for the Antarctic case). The rate of overturning slightly decreases, when runoff is included, in most of the cases in the Southern Ocean, e.g, E3k drops from ~-23 Sv to -22 Sv, while there is a slight increase in the rate of overturning in the North Pacific. The extent of the southern overturning circulation is similar whether or not runoff is included in most cases, except in E0 . In E0 the Southern Ocean overturning has become so weak that there is now a slight clockwise rotating cell in the North Pacific. In general, these results are what should be expected though. By adding runoff we have weakened the density gradient in the southern hemisphere and strengthened it in the northern hemisphere, see e.g., Fig. 25. In the 280 ppm case without runoff the southern hemisphere had the strongest gradient, but when runoff was added the density gradient was strongest in the northern hemisphere. It would then make sense for the MOC to be stronger in the North Pacific than South Pacific, which indeed it is. In the 2240k and 4480k ppm cases the decrease in the rate of overturning in the Southern Ocean is much less. Figure 25 again allows us to see why. Even with runoff added, the 2240k and 4480k cases still have a much stronger gradient in the Southern Hemisphere, with the gradient in the Northern Hemisphere almost unchanged.

Next we add runoff to the same location as before but double the rate of discharge, e.g, 32,400 m^3 s^{-1}. Figure 26 shows the results compared to a normal rate of runoff and no runoff. Doubling the runoff has caused the circulation to remain roughly the same as with the normal amount of runoff. There is a slight decrease in the rate of South Pacific sinking for the E01, E02, and E03 cases, while E0 has a slightly stronger circulation and E5k has a much weaker circulation compared to the normal rate of runoff. This can again be partially explained by the density gradient, see Welander (1971). Figure 27 shows the difference between the Southern Hemisphere maximum and minimum densities. In general, the strength of the density gradient decreased with added runoff, except E0 where the MOC happened to edge up in the Southern Ocean. E5k's southern overturning cell has largely vanished and to no surprise the strength of the density gradient has also plummeted.

Lastly, we try moving the location of the runoff to the Australian coast, see Fig. 23b. The discharge rate is the same as the original runoff case (16,200 $m^3 s^{-1}$), and everything else is kept constant. The effect on the southern overturning cells is negligible, within ~1 Sv of each other, when comparing back to the original case with no runoff. The extent of the overturning cell has also roughly remained unchanged.

In conclusion, runoff has a small affect on the MOC. The initial addition of runoff causes a slight weakening in the MOC when added into the S. Pacific. As more runoff is added the strength of the MOC slightly decreases. Moving the location of runoff from Antarctica to Australia also has little affect. In general, adding runoff does little to shift the location of deep-water from the South to North Pacific. The density gradient already favors sinking in the Southern Ocean.

5.4 Effects of seasonality

For the previous sets of model runs, surface forcing's were used that were yearly averages. The MITgcm is also capable of using boundary conditions that vary for a given time period. Therefore we felt it would be sagacious to test the sensitivity of the MOC to the effects of monthly varying boundary conditions (e.g., x and y wind stress, SST , and the E-P fields[5]). The value of mixing was kept the same ($\kappa = 0.3$ $cm^2 s^{-1}$), the

---

[5] The E-P field was rebalanced monthly

magnitude constant (c) of the E-P field was set to 0.7, and no runoff was included. Figure 28 highlights the results from simulations in which seasonality was and was not included. The rate of the Southern Pacific overturning cells remained the same in E0 and E1, while rate and extent of overturning decreased when seasonality was included in the rest of the cases. The biggest decrease in the rate of overturning was in E5k followed by E2, from -20 Sv to -6 Sv and from -24 Sv to -16 Sv respectively. The biggest decrease in the extent of overturning occurred in E3k. In E3k the overall picture of the MOC remains the same though. Sinking still occurred in the Southern Ocean in all the cases regardless of seasonality or not.

In summary, seasonality does not shift the location of deep-water formation from the Southern Ocean to the North Pacific. In the hotter greenhouse climate cases (E2 through E5), there is a reduction in the rate and extent of overturning in the South Pacific. This change in the MOC can most likely be attributed to the monthly variability in the E-P field.

6. SOUTH PACIFIC DEEP WATER: A MODE OF DEEP-WATER DURING THE LATEST CRETACEOUS AND EARLY CENOZOIC

6.1 Proxies of water mass origins

In earlier sections, we have examined the sensitivity of deep-water formation to geography and the variables that define surface boundary conditions and density distributions. In this final section, we examine simulations of the ocean circulation forced using boundary conditions derived from a previously coupled simulation (Liu et al., 2009) that is in good agreement with a synthesis of proxy evidence available from the hot climates of the Paleogene (Huber 2009; Huber and Caballero 2011). We compare the resulting water mass distributions to those inferred from Nd analysis (Thomas 2005; Hague et al., 2012; Thomas et al., 2012).

Neodymium (Nd) isotope data of water mass composition, as reviewed in the introduction, is a proxy of water mass composition. Figure 29 shows values of $\varepsilon_{Nd}(t)$ derived from Pacific Deep Sea Drilling Project (DSDP) and Ocean Drilling Program (ODP) sites 323 and 596 (in the South Pacific) and sites 463, 865, and 869 (located in the tropical Pacific). The seawater values (solid symbols and/or solid lines) are representative of deep ocean conditions at these sites, while detrital values (open symbols) indicate values from continental runoff and/or eolian dust transport.

Deep-water isotopic composition at site 323 decreased from -3.6 in the latest Cretaceous (~70 Ma) to -5.3 by ~62 Ma, which coincides with a gradual deepening of the seafloor from ~2 km to ~3 km by ~62 Ma (Hollister et al., 1976; Thomas et al. 2012). After ~62 Ma, values of $\varepsilon_{Nd}(t)$ remained between -4 and -6 into the Eocene epoch at this site. These values are similar to those from the second site located in the South Pacific (596), whose record shows a long-term stability of values from the Cretaceous (~70 Ma) through the Oligocene (~30 Ma). The similarity between records at both locations in the South Pacific suggest a common water mass source whose isotopic signature yields $\varepsilon_{Nd}(t)$ values in the -4 to -6 range.

Average deep-water $\varepsilon_{Nd}(t)$ values recorded at tropical sites 463, 865, and 869 were between -4 and -5, and those reported from sites in the North Pacific were higher still (see Figure 30; Hague et al., 2012; Thomas et al., 2012). The high $\varepsilon_{Nd}(t)$ values indicate a radiogenic source, and Hague et al. (2012) confirmed the origin of this deep-water to be the North Pacific. The decrease in $\varepsilon_{Nd}(t)$ values from north to south across the central Pacific indicates a gradual mixing with a water mass characterized with low (unradiogenic) $\varepsilon_{Nd}(t)$ values, but existing data had been unable to isolate its source.

Using Nd isotopic analyses of targeted detrital sediments, Thomas et al. (2012) have shown that this unradiogenic water mass came from the South Pacific, not the Atlantic sector of the Southern Ocean. As they report, river discharges carrying weathered rock are the dominant sources of dissolved Nd in the oceans, and these values can be measured in fine-grain detrital sediments. Yet in the open ocean (thousands of kilometers from a continental source), the only source of detrital sediments is aeolian dust.

The tropical sites (463, 596, and 869) are all in the center of the Pacific far from any land, and their detrital $\varepsilon_{Nd}(t)$ values were most likely limited to transport by wind. Moreover, the range of detrital values recorded here (-6 to -12) is consistent with contributions from unradiogenic dust, and these are all much lower than the deep-water $\varepsilon_{Nd}(t)$ values at the same sites. This suggests that the sources of the detrital sediments were different than those of deep-water. In other words, the deep-water at these tropical locations originated elsewhere.

In contrast, site 323, which is located near the Antarctic Peninsula, contains the most radiogenic detrital silicate $\varepsilon_{Nd}(t)$ values (-3.4 to -4). This peninsula contains exposed tectonostratigraphic terranes with $\varepsilon_{Nd}(t)$ values between -6 and +5 (Wareham et al., 1997; Riley et al., 2001), and weathering of these formations supplied the radiogenic detrital and dissolved Nd to the location of site 323. These values (~-4) are similar to concurrent deep-water values at the same site, indicating that the abyssal water here originated from surface waters with the same characteristics as the South Pacific surface. This relatively radiogenic signature is unique to the Pacific sector of the Southern Ocean, as $\varepsilon_{Nd}(t)$ values in the Atlantic and Indian sectors during the late Cretaceous and early Paleogene were significantly lower ($\varepsilon_{Nd}(t)$ values ~-10). Thus, the totality of this evidence strongly suggests that the source of lower deep-water Pacific values came from the Pacific sector of the Southern Ocean.

The picture that emerges from this data is one of sinking in the South Pacific Ocean, where Nd values are lower than in the North Pacific, but not as low as the Atlantic and Indian Oceans or the surface of the equatorial Pacific. The deep-water

$\varepsilon_{Nd}(t)$ values increase to the north across the Pacific Ocean, and the radiogenic Nd values found at the northern end of the basin have already been identified as a second water mass originating in deep convection at the north end of the basin (Hague et al., 2012). We next present the results of our simulations using surface conditions consistent with those from these hot periods, and compare the resulting water mass distributions with the inferences drawn from the data reviewed here.

6.2 Simulations of Pacific abyssal circulation

We restored the surface temperature and salinity values to those shown in Figure 31 (except our actual model was fed seasonally varying values, rather than the annual means presented in the figure) and used the wind stress in equilibrium with the fields to drive the MITgcm. The annual mean SST field (Fig. 31a) has a minimum temperature of about 6°C around the Antarctic coast, and a maximum temperature of ~35°C in the tropics just southwest of the present day tip of the Asian continent. The North Pacific has a minimum temperature of approximately 14°C. The sea surface salinity (SSS) field (Fig. 31b) has peaks of ~39 ppt in both subtropical bands of 30°N/S, with minima in the South and North Atlantic Oceans, ~26 ppt. The evaporation field (Fig. 31c) features two bands of significant evaporation in the subtropics (in the subsidence region of the Hadley Cell) of about 2 m yr^{-1}, and minima around the Polar Regions. It is important to note that the evaporation field is not perfectly symmetric about the equator. The precipitation field (Fig. 31d) has a maximum of about 8 m yr^{-1} around present day India, with a band of high precipitation, ~3 m yr^{-1}, near the equator from tropical convection. Continental runoff (Fig. 31e) occurs in isolated bursts, including a large discharge off the coast of Africa (8 m yr^{-1}) and other significant inputs off the north coast of the South American continent, and the Antarctic coast. The surface wind speed (Fig. 31f) has peaks in four areas: two low latitude trade wind bands (~ 15°N/S) blowing from east to west and mid-latitude westerlies, owing to storm tracks, at ~50°N/S. The Southern Hemisphere westerlies are stronger than the Northern Hemispheric ones.

The SST field for E4 (4480 ppm/ Fig. 32a) is warmer around the globe. There is a temperature maximum of ~38°C in the tropics just southwest of the tip of present day Asia, compared to ~35°C for the E3 case. The minimum temperature in the North Pacific has risen from 14°C to 20°C, and the South Pacific temperature has risen from 6°C to 15°C. The SSS field (Fig. 32b) has also slightly risen in the subtropics, with maximum salinity values reaching 41 ppt compared to 39 ppt. The magnitudes of the evaporation field (Fig. 32c) remain about the same, but the 2 m yr^{-1} contour in the subtropics has expanded to fill almost the entire subtropical region, ~10°N/S to 20°N/S. The precipitation field (Fig. 32d) remains similar to that of E3 except that the maximum precipitation value now occurs off the southeastern tip of present day Asia. The surface wind speed magnitude (Fig. 32d) decreases for an increasingly warmer climate. The pattern is about the same though. The maximum wind speed occurs off the west coast of South America, with stronger wind speeds generally occurring in the Southern Hemisphere compared to the Northern Hemisphere.

With these fields, water sinks at both ends of the Pacific Ocean, a pattern that persists using data from hotter conditions (Figure 32) and bulk forcing boundary conditions (Large et al. 1997).

From these two sets of boundary conditions the model was run until equilibrium and the MOC was then calculated (Figure 33). The MOC for the Pacific basin for both E3 (Fig. 33a) and for E4 (Fig. 33b) are shown. In between the dashed grey lines the MOC is averaged from the African coast across the Pacific Ocean to the South American continent. The South Pacific MOC for E3 has a moderate overturning strength, ~-9 Sv, with the water sinking all the way to the bottom of the ocean. The North Pacific for E3 has a slightly higher rate of overturning of 17 Sv with the water mass only able to sink to ~2000 m deep thanks to the denser water of the South Pacific underneath. The E4 case does not have to many differences. The rate of overturning has slightly decreased in the South Pacific, from -9 to -7 Sv, but the extent of South Pacific deep-water (SPDW) has slightly increased though. The entire floor of the Pacific Ocean carries the SPDW signature, and the cell in the South Pacific has increased in strength around 50°S. The North Pacific sinking region remains roughly the same in rate and extent of overturning.

6.3 Nd tracer distributions

The deep-water $\varepsilon_{Nd}(t)$ values from the various cores shown in Figure 29 were derived from fish teeth buried on the ocean floor, and hence are representative of the $\varepsilon_{Nd}(t)$ values at the sea floor at time of burial. The sites in the tropical Pacific (463, 865, and 869) were located at various depths, so the values from each have the potential to provide some information about the vertical distribution through the water column at these latitudes. Site 865 was located on the Mid-Pacific mountains and was the shallowest of the three locations (the sea floor here was ~1500 m deep). Sites 463 and 869 were deeper: ~2000 and ~3600 m, respectively. All of these lie beneath the thermocline in the modern ocean, and are embedded in the abyssal flows of our simulations too. Yet it is interesting to note that site 865, which is the shallowest, has higher $\varepsilon_{Nd}(t)$ values than does 869, which is also located near the equator, but at substantially greater depth. If this is representative, it would indicate a more radiogenic water mass at shallower depths, with a less radiogenic source dominating parcels that lie underneath.

Neodymium can be regarded, essentially, as a passive tracer owing to its long lifetime in the ocean. As reviewed in the introduction, its lifetime is ideally suited to be used as a water mass tracer, as it is long enough so that water retains the signal it was first assigned at the surface from river discharges, surface currents, and advection by wind, but not so long that ancient values are permanently imprinted once deep water returns to the surface.

We ran a passive tracer that restores instantaneously to the surface distribution shown in Figure 34a. Though simple, this distribution reflects surface values known to exist in the South Pacific (-6; Thomas et al., 2012) and North Pacific (+10; Hague et al., 2012). Elsewhere, unradiogenic values (-10) are assigned in the central Pacific and all of the Indian and Atlantic sectors. As we show, the wide uncertainty in surface values in remote locations is unimportant to the Pacific interior distributions, so long as the surface values where deep-water forms are reasonably well known.

Figure 35 shows the resulting passive tracer distribution zonally averaged from 152°W to 148°E for the E3 case. Panel a is restored to the surface values shown in Fig. 34a. Panel b restores to the values in Fig. 34b. The interior distributions of both Fig. 34a and b are identical below 1000m. The initial conditions at the surface around the equator do not affect the final tracer outcome here. In both panels the unradiogenic values of the South Pacific (-6) have flooded the entire seafloor, while more radiogenic values from the North Pacific (+10) mix with the ambient values in higher portions of the tropical water columns. In summary, the North Pacific water is less dense intermediate water, North Pacific Intermediate Water (NPIW), with the denser SPDW underneath it. Our tracer results agree with the data described above, a SPDW signature throughout the floor of the ocean with a higher more radiogenic NPIW above it. Figure 36 shows the resulting tracer distributions for the E4 case. Again, our results show that the final tracer distribution is independent of the surface equatorial Nd values, so long as values at sinking regions are known. Also, the interior ocean values are almost unchanged from the E3 case, a SPDW source that can be found throughout the seafloor of the Pacific, with a less dense NPIW source found above it.

7. SUMMARY AND CONCLUSIONS

We used the MITgcm model to determine how altering various surface boundary conditions changed the location of deep-water formation. First, we looked at results from Idealized bathymetry in which the effects of open passageways was tested. We then analyzed how changing the temperature gradient, the wind stress, and the mixing affected the MOC. We started with present day temperature gradients and wind stress profiles and then performed modifications to them. Next, cases were presented that used realistic bathymetry. In these model simulations, output from seven different CAM3 runs was used to force the MITgcm: 280 ppm (E0), 560 ppm (E1), 1120 ppm (E2), 2240 ppm (E3), 2240 ppm with constant SST (E3k), 4480 ppm (E4k), and 8960 ppm (E5k), where cases that don't have a k prefix were coupled to a slab ocean and cases with a k prefix had prescribed SST's. First, the addition of salinity was tested to see how the MOC was altered. Finally, the effects of runoff and seasonality on the location of deep-water formation was tested. In the last section we determined how sensitive the sinking of deep-water was to different places in the Southern Ocean, and how this alters maps of tracer reconstructions. Finally, altering the initial surface tracer distribution was tested to see if this could alter the final result.

This study has captured a couple of major concepts. First, the idealized bathymetry was used to help verify some basic physical principles given imposed density fields. In particular, given a set density field, water will generally sink where it is closest to the poles. This is because, when not including the effects of salinity, temperature was set to decrease the farther poleward one traveled, i.e., polar regions were the most dense. The point was also demonstrated using various geometric configurations. The ocean basin that went farthest poleward was generally the one that had deep- water formation occurring in it, again because it had the densest water. We also showed that the depth of the CAS had little change on the MOC. The presence of a passageway itself did though change the extent of the MOC. Second, using the realistic bathymetry it is shown that south pacific sinking occurs across a wide range of parameters. The location of where in the Southern Ocean deep-water forms is much more sensitive to the surface boundary conditions tested. Tracer reconstructions are also quite sensitive to this, along with the initial surface distribution of the tracer. Model simulations that try and reconstruct tracer distributions and compare them to proxy derived tracer distributions need to be aware of this. In studies that can estimate ε_{Nd} values during the early Cenozic, our model-derived simulations match up when sinking occurred in the South Pacific. When sinking occurred elsewhere, in our study was about half of our results, the final tracer distributions were different.

We showed that an ocean model forced with surface conditions consistent with available proxy evidence from the early Cenozoic produces two deep-water masses originating at both ends of the Pacific. The resulting overturning circulation and tracer distributions are consistent with the interpretation of data from deep sea cores: that a water mass originating in the radiogenic North Pacific mingled with an unradiogenic source from the Pacific sector of the Southern Ocean (Thomas et al., 2012). The consistency of the picture produced by Nd isotopic analysis and the general circulation model results synergistically boost confidence in the interpretation: models appear able to reproduce features of the MOC in the early Paleogene, which provides some confidence that the near-modern circulation and heat transport rates they produce are likely correct.

REFERENCES

Ali, J. R., and M. Huber (2010), Mammalian biodiversity on Madagascar controlled by ocean currents, *Nature, 463*, 653-657.

Barron, E. J. (1987), Eocene equator-to-pole surface ocean temperatures: A significant climate problem, *Paleoceanography, 2* (6), 729-739.

Barron, E. J., and W. H. Peterson (1991), The Cenozoic ocean circulation based on ocean General Circulation Model results, *Palaeogeography, Palaeoclimatology, Palaeoecology, 83*, 1-28.

Bice, K. L., and J. Marotzke (2001), Numerical evidence against reversed thermohaline circulation in warm Paleocene/ Eocene Ocean, *Journal of Geophysical Research, 106* (C6), 11529- 11542.

Bice, K. L., and J. Marotzke (2002), Could changing ocean circulation have destabilized methane hydrate at the Paleocene/ Eocene boundary, *Paleoceanography, 17* (2), 8-1 : 8-9.

Bijl, P. K., S. Schouten, A. Sluijs, G.-J. Reichart, J.C. Zachos, and H. Brinkhuis (2009), Early Palaeogene temperature evolution of the southwest Pacific Ocean, *Nature, 461*, 776-779.

Bryan, K., and L. J. Lewis (1979), A water mass model of the world ocean, *Journal of Geophysical Research, 84* (C5), 2503-2517.

Caballero, R., and M. Huber (2010), Spontaneous transition to superrotation in warm climates simulated by CAM3, *Geophysical Research Letters, 37* (L11701), 1-5.

Cox, M. D., and K. Bryan (1984), A numerical model of the ventilated thermocline, *Journal of Physical Oceanography, 14,* 674-687.

Danabasoglu, G., and J. C. McWilliams, 1995: Sensitivity of the global ocean circulation to parameterizations of mesoscale tracer transports, *Journal of Climate, 8,* 2967-2987.

DePaolo, D., and G. Wasserburg (1976), Nd isotopic variations and petrogenetic models, *Geophysical Research Letters, 3* (5), 249-252.

Elderfield, H., and M. J. Greaves (1982), The rare earth elements in seawater, *Nature, 296*, 214-219.

Ferrari, R., and C. Wunsch (2004), Vertical mixing, energy, and the general circulation of the oceans, *Annu. Rev. Fluid Mech., 36*, 281-314.

Gent, P. R., and C. J. McWilliams (1990), Isopycnal mixing in ocean circulation models, *Journal of Physical Oceanography, 20*, 150-155.

Gent, P. R., J .Willebrand, T. J. McDougall, and J. C. McWilliams (1995), Parameterizing eddy- induced tracer transports in ocean circulation models, *Journal of Physical Oceanography, 25*, 463-474.

Goldstein, S. J., and S. B. Jacobsen (1988), Nd and Sr isotopic systematics of river water suspended material: implications for crustal evolution, *Earth and Planetary Science Letters*, 249- 265.

Hague, A. M., D. J. Thomas, M. Huber, R. Korty, S. Woodard, and L. B. Jones (2012), Convection of north pacific deep water during the early Cenozoic, *Geology*, in press.

Halliday, A. N., J. P. Davidson, P. Holden, R. M. Owen, and A. M. Olivarez (1992), Metalliferous sediments and the scavenging residence time of Nd near hydrothermal vents, *Geophysical Research Letters, 19* (8), 761-764.

Hellerman, S., and M. Rosenstein (1983), Normal monthly wind stress over the World Ocean with error estimates, *Journal of Physical Oceanography, 13*, 1093-1104.

Hollis, C. J., L. Handley, E. M. Crouch, H. E. Morgans, J. A. Baker, J. Creech, et al. (2009), Tropical sea temperatures in high-latitude south pacific during the Eocene, *Geology, 37* (2), 99-102.

Hollister, C.D., C. Craddock, Y. Bogdanov, N. Edgar, J. Gieskes, et al., (1976), *Init. Rep. DSDP, 35*: Washington D.C., U.S. Government Printing Office, 930 p.

Huber, M., and L. C. Sloan, (2001), Heat transport, deep waters, and thermal gradients: Coupled simulation of an Eocene greenhouse climate, *Geophysical Research Letters, 28* (18), 3481-3484.

Huber, M., H. Brinkhuis, C. E. Stickley, K. Döös, A. Sluijs, J. Warnaar, et al. (2004), Eocene circulation of the Southern Ocean: Was Antarctica kept warm by subtropical waters, *Paleoceanography, 19* (PA4026), 1-12.

Huber, M. (2008), A hotter greenhouse, *Science, 321*, 353-354.

Huber, M. (2009), Snakes tell torrid tale. *Nature, 457,* 669-671.

Huber, M., and R. Caballero (2011), The early Eocene equable climate problem revisited, *Climate of the Past, 7*, 603-633.

Jackett, D. R., and T. J. McDougall (1995), Minimal adjustment of hydrographic profiles to achieve static stability, *Journal of Atmopsheric and Oceanic Technology*, 381-389.

Jones, C. E., A. N. Halliday, D. K. Rea, and R. M. Owen (1994), Neodymium isotopic variations in north pacific modern silicate sediment and the insignifigance of detrital REE contributions to seawater, *Earth and Planetary Science Letters, 127*, 55- 66.

Kammerer, J.C. (May 1990), Largest rivers in the United States, *U.S. Geological Survey*, http://pubs.usgs.gov/of/1987/ofr87-242/, Retrieved 2012-03-20.

Korty, R. L. (2005), On the maintenance of weak meridional temperature gradients during warm climates. Ph.D. dissertation, Massachusetts Institute of Technology, Earth, Atmospheric and Planetary Sciences. Cambridge, MA.

Lyle, M. (1997), Could early Cenozoic thermohaline circulation have warmed the poles, *Paleoceanography, 12* (2), 161-167.

Large, W. G., G. Danabasoglu, S. C. Doney, and J. C. McWilliams (1997), Sensitivity to surface forcing and boundary layer mixing in a global ocean model: Annual mean climatology, *Journal of Physical Oceanography, 27*, 2418-2447.

Liu, Z., M. Pagani, D. Zinniker, R. DeConto, M. Huber, H. Brinkhuis, et al. (2009), Global cooling during the Eocene- Oligocene climate transition, *Science, 323*, 1187-1190.

Livermore, R., A. Nankivell, G. Eagles, and P. Morris (2005), Paleogene opening of Drake Passage, *Earth and Planetary Science Letters, 236*, 459-470.

Nilsson, J., and G. Brüstrom (2003), The thermohaline circulation and vertical mixing: Does weaker density stratification give stonger overturning, *Journal of Physical Oceanography*, 2781-2795.

Nunes, F., and R. D. Norris (2006), Abrupt reversal in ocean overturning during the Palaeocene/ Eocene warm period, *Nature, 439*, 60 - 63.

Marotke, J. (1989), Instabilities and multiple steady states of the thermohaline circulation, In E. K. D.L.T. Anderson and J. Willebrand, *Ocean Circulation*

Models: Combining Data and Dynamics (pp. 501 -511). Les Houches, France: Kluwer.

Marshall, J., A. Adcroft, C. Hill, L. Perelman, C. and Heisey (1997a), A finite-volume, incompressible Navier Stokes model for studies of the ocean on parallel computers, *Journal of Geophysical Research, 102* (C3), 5753 - 5766.

Marshall, J., C. Hill, L. Perelman, and A. Adcroft (1997b), Hydrostatic, quasi-hystrostatic, and nonhydrostatic ocean modeling, *Journal of Geophysical Research, 102* (C3), 5733-5752.

Molnar, P. (2008), Closing of the Central American Seaway and the Ice Age: A critical review, *Paleoceanography, 23*, PA2201.

Müller, R. D., M. Sdrolias, C. Gaina, and W. R. Roest (2008), Age, spreading rates, and spreading asymmetry of the world's ocean crust, *Geochemistry, Geophysics, Geosystems, 9* (4), 1-19.

Pearson, P. N., P. W. Ditchfield, J. Singano, K. G. Harcourt- Brown, C. J. Nicholas, R. K. Olsson, et al. (2001), Warm tropical sea surface temperatures in the late Cretaceous and Eocene epochs, *Nature, 413*, 481-487.

Peixoto, J. P., and A. H. Ort (1992), *Physics of Climate.* New York, NY: Springer-Verlag.

Riley, T., P. Leat, R. Pankhurst, C. Harris (2001), Origins of large volume rhyolitic volcanism in the Antarctic Peninsula and Patagonia by crustal melting, *Journal of Petrology, Vol. 42,* 1043-1065.

Schrag, D. P. (1999), Effects of diagenesis on the isotopic record of late paleogene tropical sea surface temperatures, *Chemical Geology*, 215-224.

Sluijs, A., S. Schouten, M. Pagani, M. Woltering, H. Brinkhuis, J. S. Sinninghe Damsté, et al. (2006), Subtropical Arctic Ocean temperatures during the Palaeocene/ Eocene thermal maximum, *Nature, 441*, 610-613.

Stewart, R. H. (2005), *Introduction to Physical Oceanography*. College Station, TX, http://oceanworld.tamu.edu/resources/ocng_textbook/ contents.html.

Stott, L. D., J. P. Kennett, N. J. Shackleton, and R. M. Corfield (1990), The evolution of Antarctic surface waters during the Paleogene: Inferences from the stable isotopic composition of planktonic foraminifers, ODP Leg 113, *Proceedings of the Ocean Drilling Program, Scientific Results , 113*.

Tachikawa, K., C. Jeandel, and M. Roy- Barman (1999), A new approach to the Nd residence time in the ocean: The role of atmospheric inputs, *Earth and Planetary Science Letters*, 433-446.

Thomas, D. J. (2005), Reconstructing ancient deep-sea circulation patterns using the Nd isotopic composition of fossil fish debris, *Geological Society of America Special Paper, Special Paper 395*, 1-11.

Thomas, D. J., M. Lyle, T. C. Moore Jr., and K. D. Rea (2008), Paleogene deepwater mass composition of the tropical pacific and implications for thermohaline circulation in a greenhouse world, *Geochemistry, Geophysics, Geosystems , 9* (2), 1-13.

Thomas, D. J., J.A. Schubert, B. Haines, R. Korty, M. Huber (2012), Pacific deep-water circulation separate from atlantic during the latest Cretaceous- early Cenozoic, submitted.

Tziperman, E., J. R. Toggweiler, Y. Feliks, and K. Bryan (1994), Instability of the thermohaline circulation with respect to mixed boundary conditions: Is it really a problem for realistic models, *Journal of Physical Oceanography, 105,* 217-232.

Vallis, G. K. (2006). *Atmospheric and Oceanic Fluid Dynamics.* Princeton University, New Jersey, USA: Cambridge University Press.

Von der Heydt, A., and H. A. Dijkstra (2006), Effect of ocean gateways on the global ocean circulation in the late Oligocene and early Miocene, *Paleoceanography, 21*, 1- 18.

Von der Heydt, A., and H. A. Dijkstra (2008), The effect of gateways on oceaen circulation patterns in the Cenozoic, *Global and Planetary Change*, 132-146.

Weaver, A. J., and E. S. Sarachik (1991), Evidence for decadal variability in an ocean general circulation model: An advective mechanism, *Atmosphere- Ocean, 29:2*, 197-231.

Weaver, A. J., E. S. Sarachik, and J. Marotzke (1991), Freshwater flux forcing of decadal and interdecadal oceanic variability, *Nature, 353*, 836- 838.

Welander, P. (1971), The thermocline problem, *Phil. Trans. R. Soc. Land. A. , 30-2*, 415-421.

Wareham, C.D., I. L. Millar, A. P. M. Vaughan (1997), The generation of sodic granite magmas, western palmer land, Antarctic peninsula and patagonia by crustal melting, Contrib. Mineral. Petrol., 128*,* 81-96.

Wright, J. D., and K. G. Miller (1993), Southern Ocean influcences on late Eocene to Miocene deepwater circulation, *The Antarctic Paleoenvironment, 60*, 1-25.

Zachos, J. C., L. D. Stott, and K. C. Lohmann (1994), Evolution of early Cenozoic marine temperatures, *Paleoceanography*, 353-387.

Zachos, J., M. Pagani, L. Sloan, E. Thomas, and K. Billups (2001), Trends, rythms, and aberrations in global climate 65 Ma to present, *Science, 292*, 686-693.

APPENDIX A

TABLES

Table 1: Summary of boundary conditions for results presented in section 4.

Thesis Section	MOC (Fig. #)	Bathymetry (Fig. #)	Zonal Wind Stress (Fig. #)	SST Relaxation (Fig. #)	κ ($cm^2 s^{-1}$)	Bryan Lewis (Fig. #)
4.1	6	5	2	3	0.3	N/A
4.1	8	7a	2	3	0.3	N/A
4.1	N/A	7b	2	3	0.3	N/A
4.1	N/A	7c	2	3	0.3	N/A
4.1	9	7d	2	3	0.3	N/A
4.2	N/A	7d	2	10 ($\Delta T = 25$°C)	0.3	N/A
4.2	N/A	7d	2	10 ($\Delta T = 39$°C)	0.3	N/A
4.2	N/A	7d	2	10 ($\Delta T = 12$°C)	0.3	N/A
4.2	12	7d	2	11 (Temp = +5)	0.3	N/A
4.2	12	7d	2	11 (Temp = +7)	0.3	N/A
4.2	12	7d	2	11 (Temp = +5)	0.3	N/A
4.2	12	7d	2	11 (Temp = +2.5)	0.3	N/A
4.2	12	7d	2	11 (Temp = +0)	0.3	N/A
4.2	12	7d	2	11 (Temp = -4)	0.3	N/A
4.3	12	7d	13 (τ)	3	0.3	N/A
4.3	12	7d	13 ($2*\tau$)	3	0.3	N/A
4.3	12	7d	13 ($0.5*\tau$)	3	0.3	N/A
4.3	12	7d	13 (North Shift τ)	3	0.3	N/A
4.3	12	7d	13 (South Shift τ)	3	0.3	N/A
4.4	N/A	7d	2	3	0.3 (surface) / 1.5 (deep)	15
4.4	16	7c	2	3	0.3 (surface)/ 1.5 (deep)	16

APPENDIX B

FIGURES

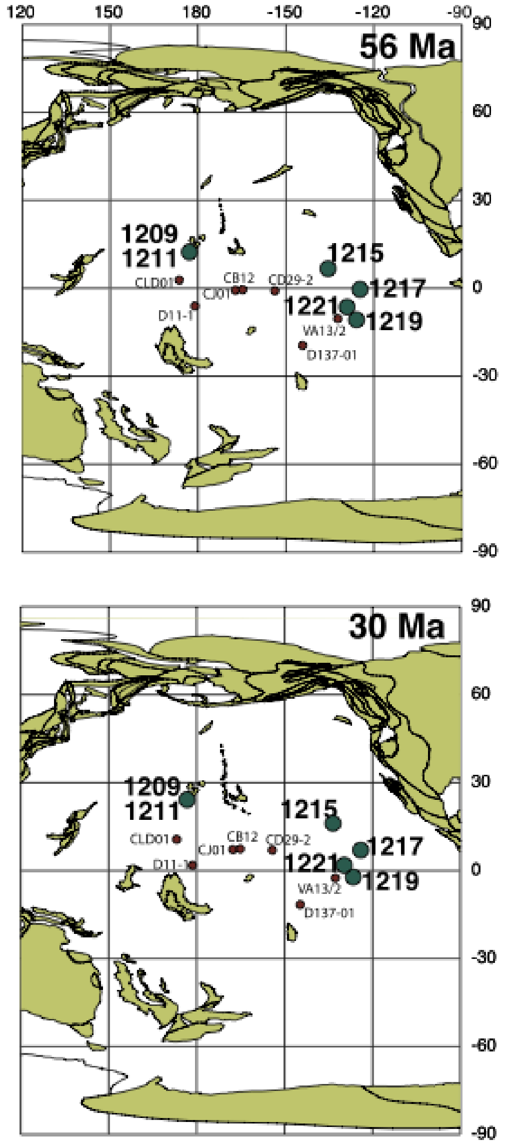

Figure 1: Station location for ε_{Nd} ratio. From Thomas et al., 2008.

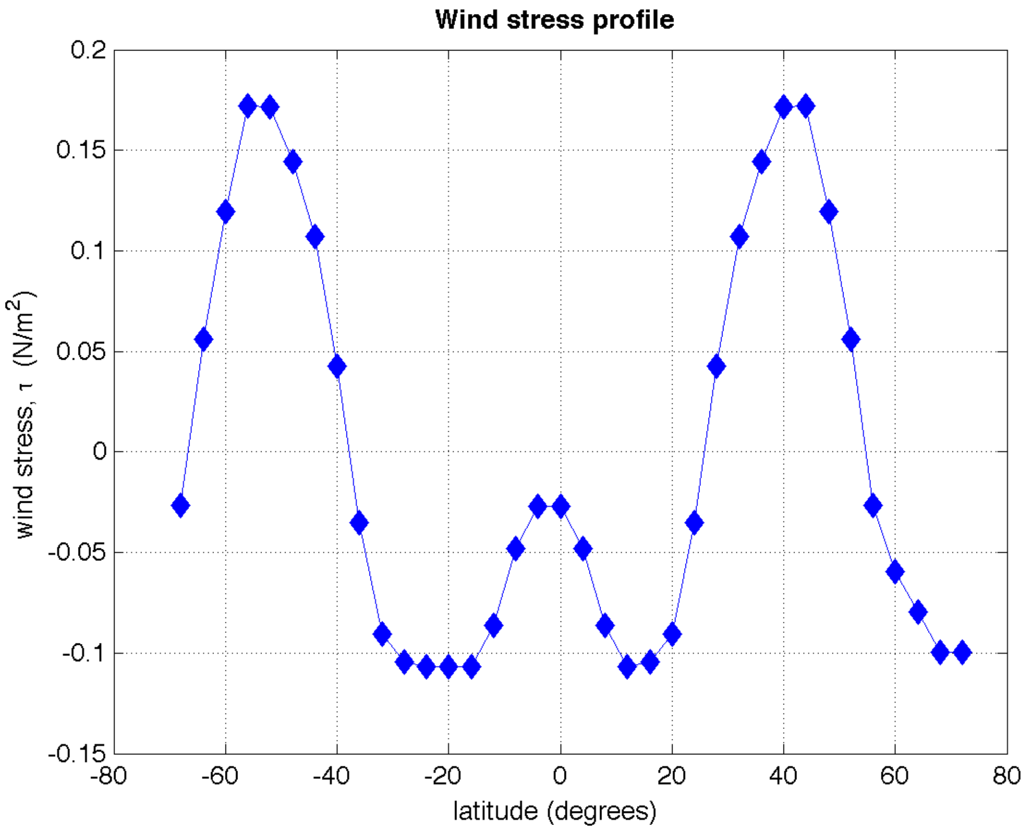

Figure 2: Initial wind stress profile applied to the model. Diamonds are plotted at each actual grid point.

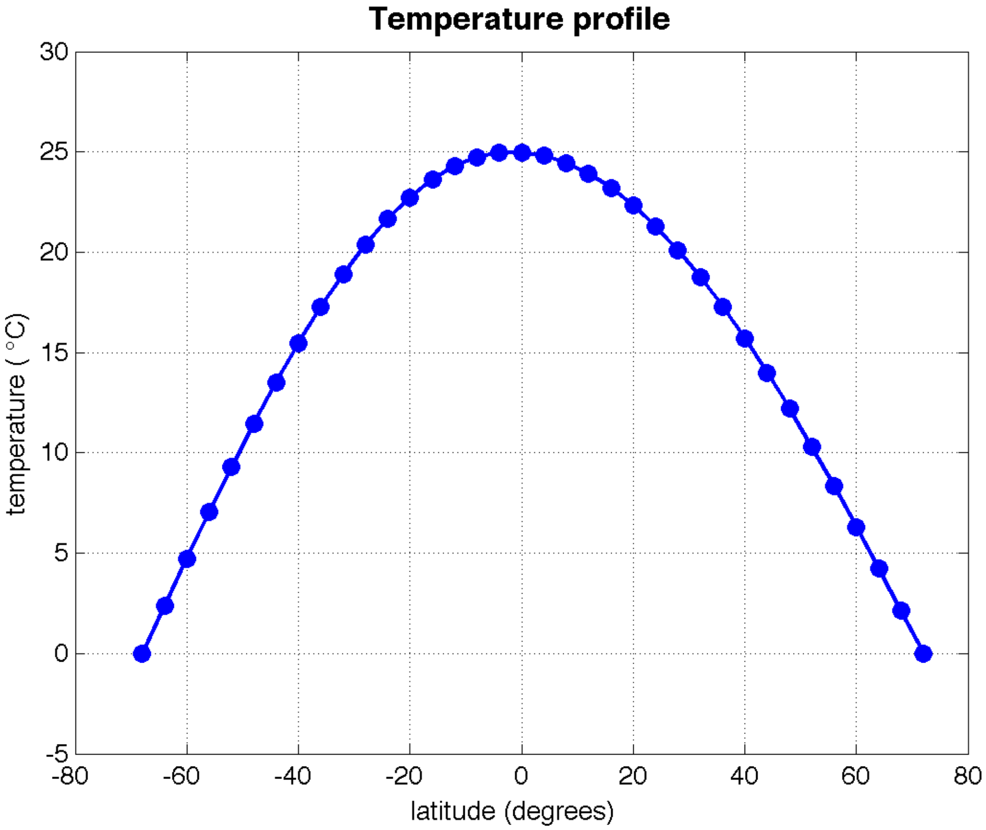

Figure 3: Initial surface temperature profile applied to the model. The surface temperature (density) field is restored (diamonds are plotted at each actual grid point) in the idealized bathymetry model simulations.

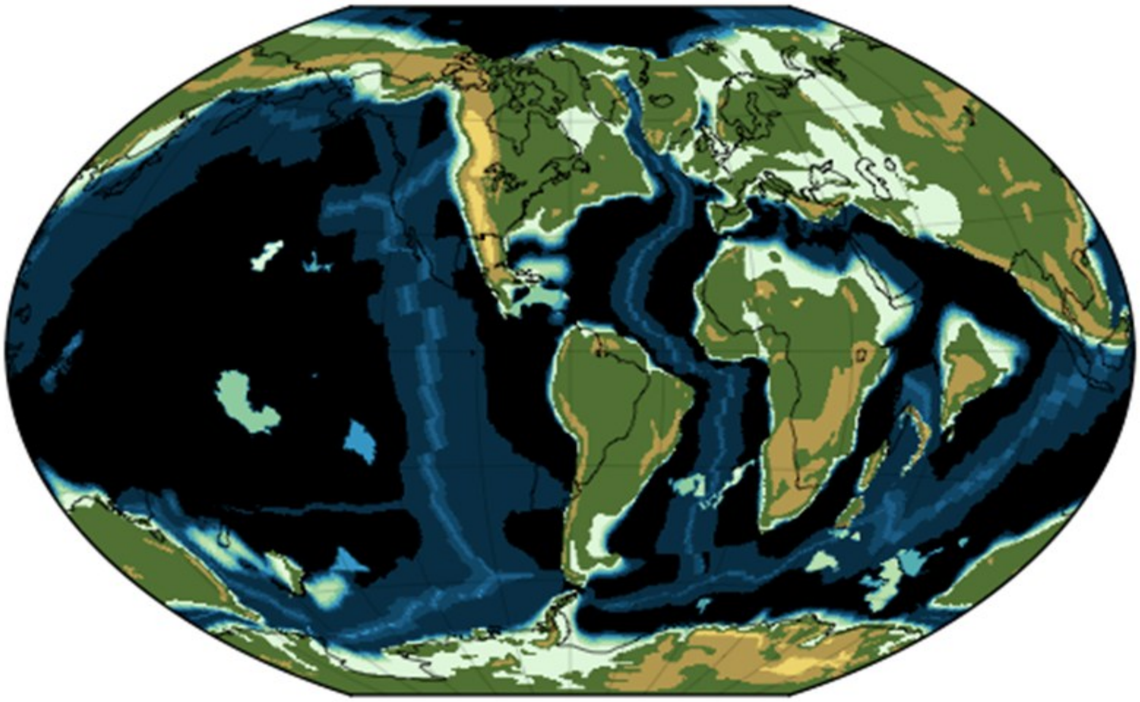

Figure 4: Reconstruction of Eocene topography. Eocene topography can be found in color with present-day topography outlined in black. Eocene bathymetry is also colored in. Courtesy of Matt Huber.

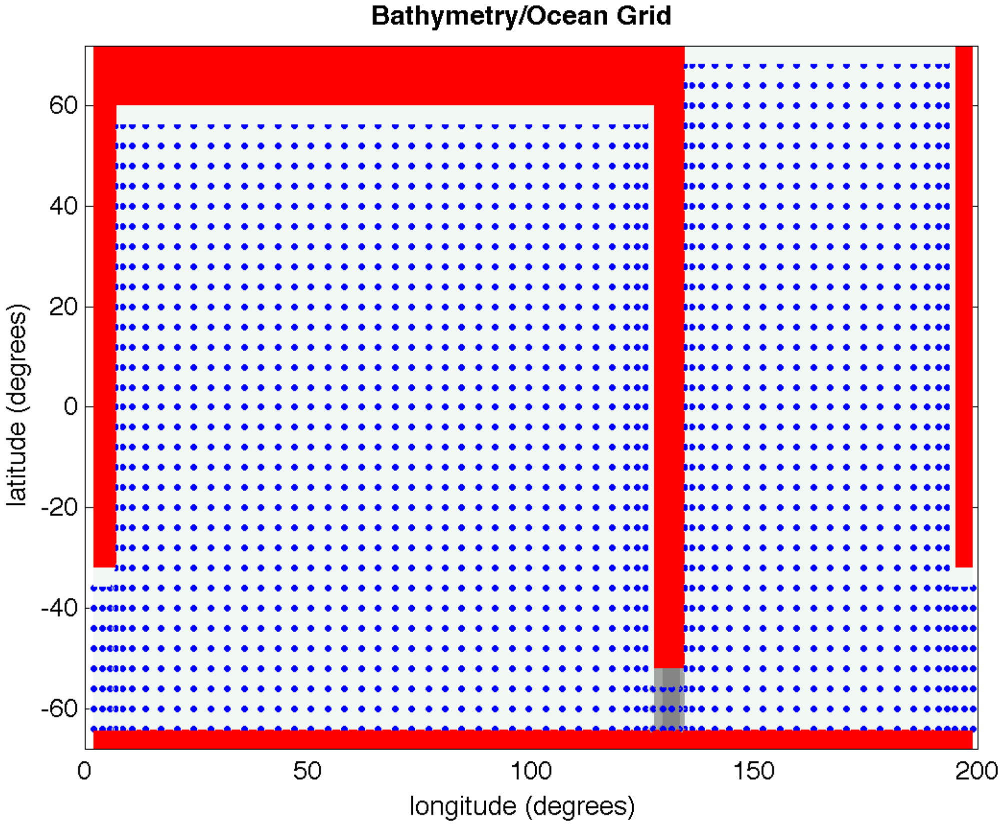

Figure 5: Ocean model grid for present day. The red color represents a depth of 0 (i.e. land) and the grey shading represents a sill of 3320m, for the Drake Passage. The white color represents an ocean depth of 4500m. For the bathymetry there is a Pacific- Indian basin (left), extending to 60°N, connected to a long, narrow Atlantic basin (right) by a band of points circling the globe.

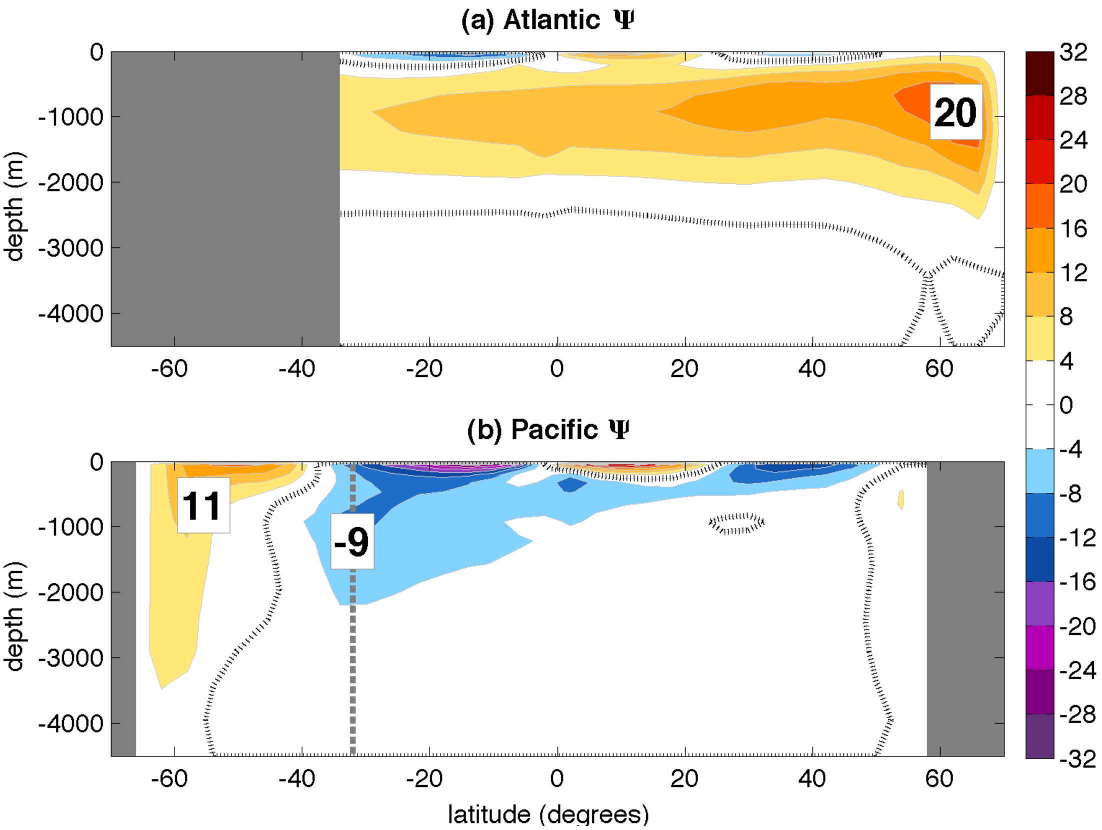

Figure 6: MOC for present day idealized topography. The topography can be found in Figure 5. Panel (a) shows the strength of the MOC of the Atlantic Ocean in Sv. Panel (b) shows the strength of the MOC of the Pacific Ocean in Sv. Note that in (b), numbers south of the vertical dashed grey line, at 32°S, are averaged around the globe.

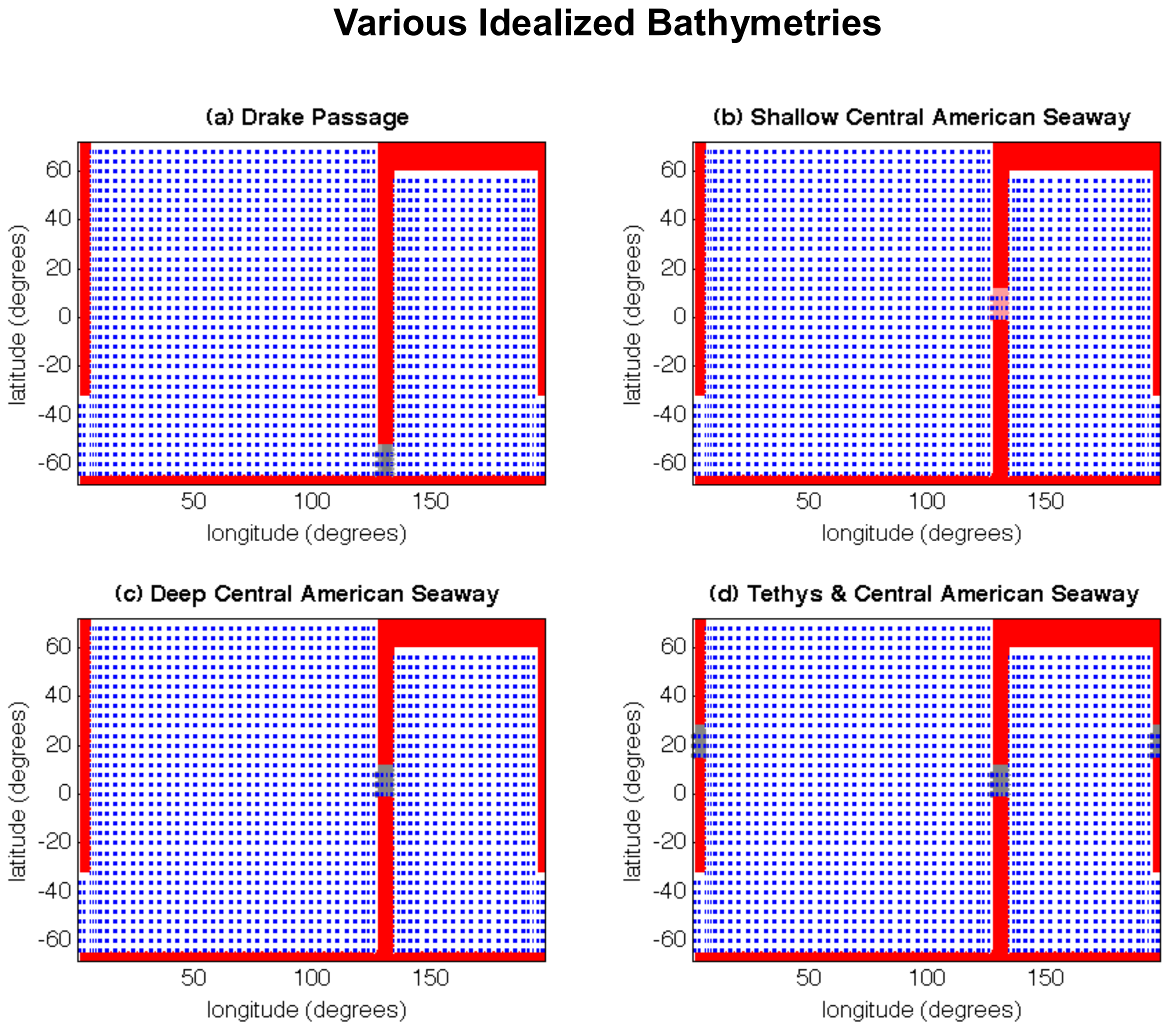

Figure 7: Various idealized ocean basin bathymetries. Panel (a) illustrates present day topography with a taller Pacific Ocean and a shorter Atlantic Ocean. Panels (b & c) illustrate an opening in Panama with depths of 1000m and 3000m respectively. Panel (d) has an opening in both Panama (3000m) and in the Tethys Sea (3000m). Ocean grid spacing is the same as in Figure 5 for all panels.

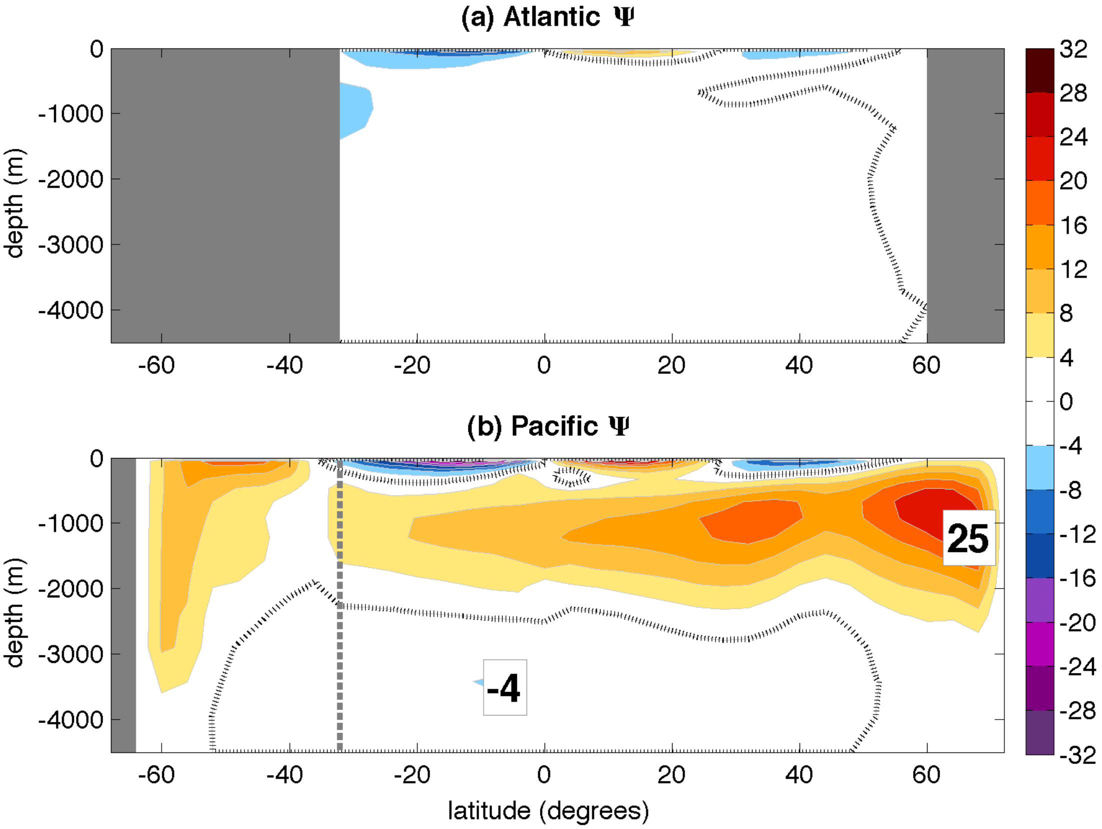

Figure 8: MOC for the topography in Figure 7a. Panel (a) shows the strength of the MOC of the Atlantic Ocean in Sv. Panel (b) shows the strength of the MOC of the Pacific Ocean in Sv. Note that in panel (b) numbers south of the vertical dashed grey line, at 32°S, are averaged around the globe.

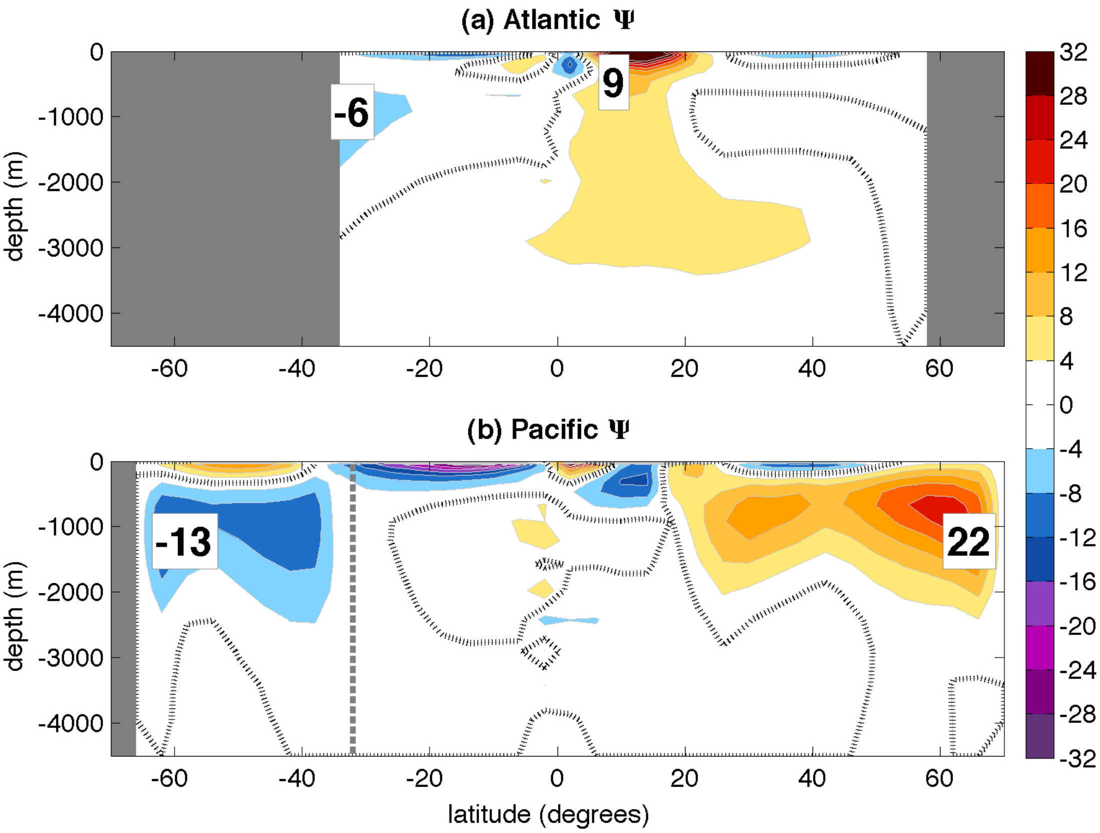

Figure 9: MOC for the topography seen in Figure 7d. Panel (a) shows the strength of the MOC of the Atlantic Ocean in Sv. Panel (b) shows the strength of the MOC of the Pacific Ocean in Sv. Note that in panel (b) numbers south of the vertical dashed grey line, at 32°S, are averaged around the globe.

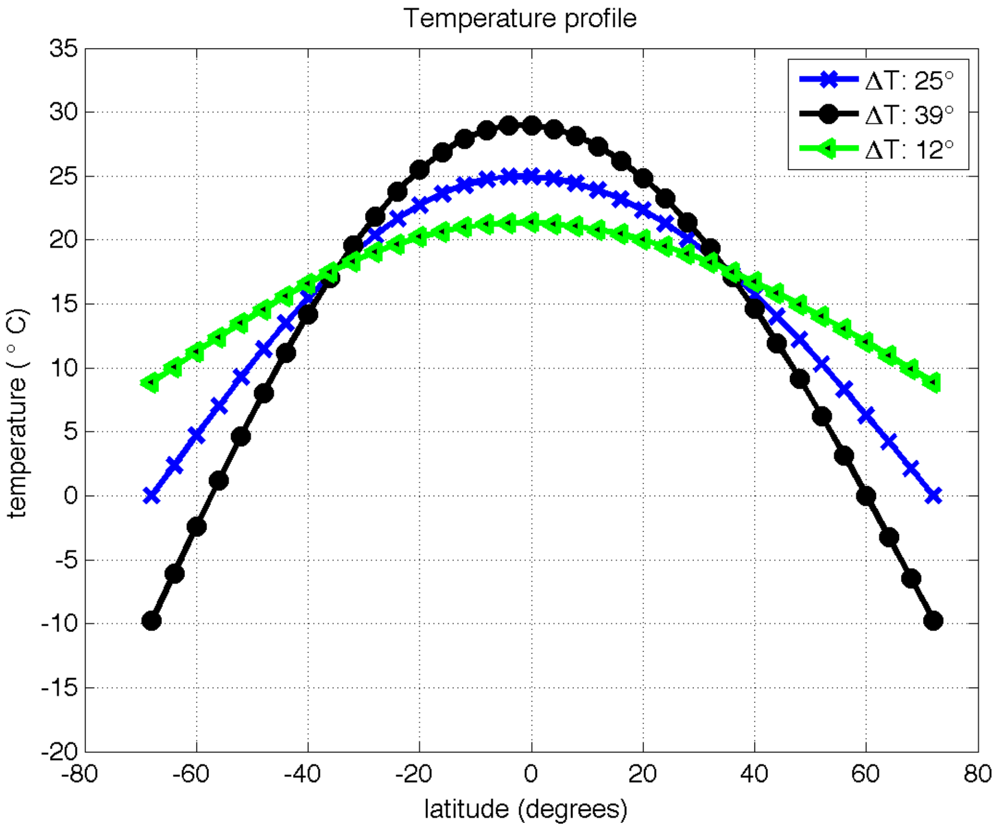

Figure 10: Temperature profile for varying gradient magnitudes. The temperature profile to which the surface temperature (density) field is restored (points are plotted at each actual grid point). The blue line is the control run temperature gradient. From the control gradient a larger temperature gradient (ΔT: 39°) and a smaller gradient (ΔT: 12°) was created. The topography used for this set of model runs can be found in Figure 7d.

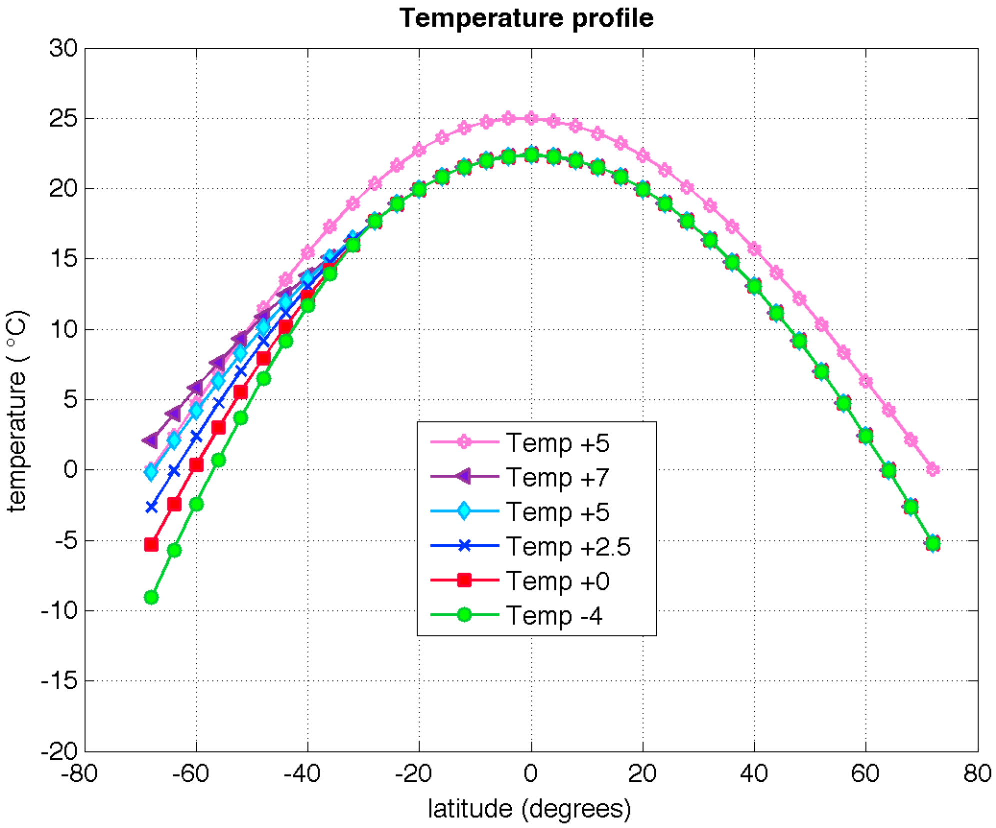

Figure 11: Temperature profile for varying gradient symmetries. The temperature profile to which the surface temperature (density) field is restored (points are plotted at each actual grid point). From 32°S northward, the temperature gradient is the same for the different cases. Southward of 32°S the gradient was altered from Temp +2.5, both colder and warmer. The control run test gradient, Temp +5 (pink line), is also plotted for reference. The topography used for this set of model runs can be found in Figure 7d.

(a) Maximum Ψ in the North Pacific

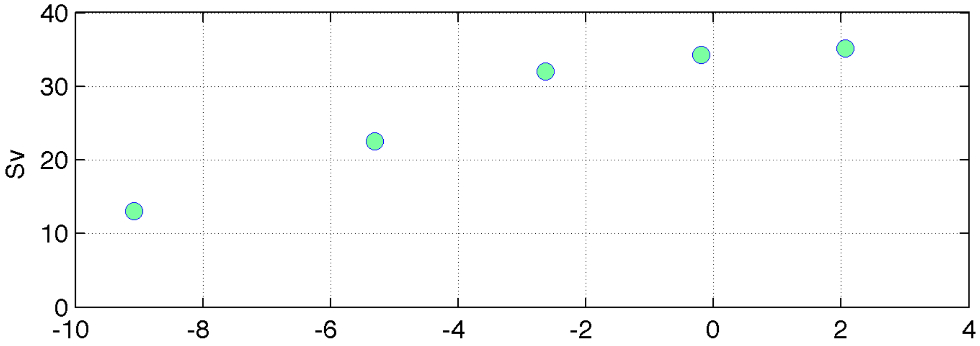

(b) Maximum Ψ in the South Pacific

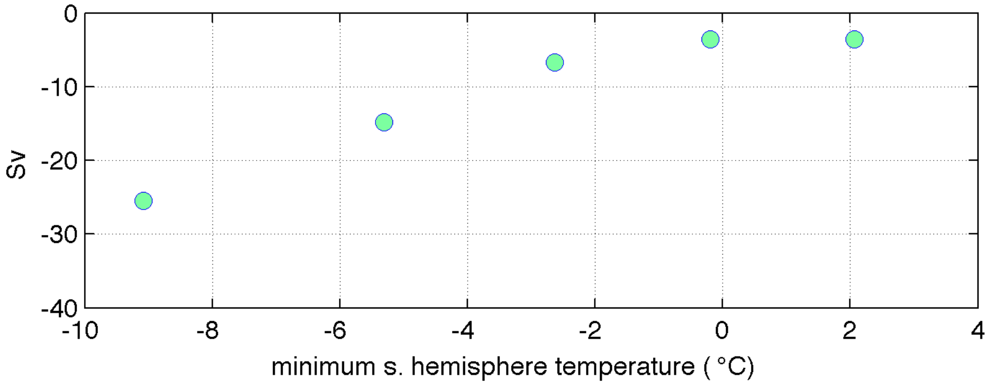

Figure 12: MOC summary for results from Figure 11. (a) Maximum ψ in the North Pacific from simulations in which ΔT was changed poleward of 32°S, see Figure 11. (b) Maximum ψ in the South Pacific from simulations in which ΔT was changed poleward of 32°S.

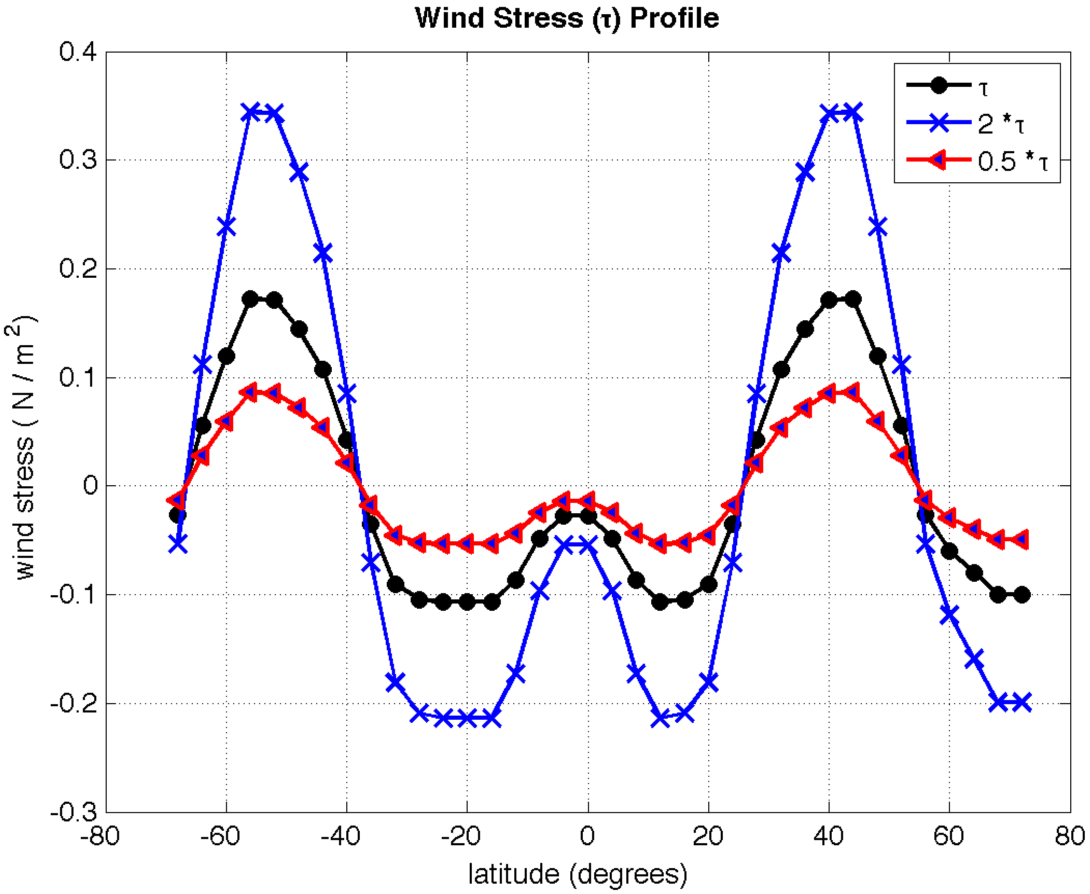

Figure 13: Wind stress profile for varying magnitudes. The wind stress profiles applied to the model (markers are plotted at each actual grid point). The original wind stress profile is plotted in black while two times the original wind stress (blue line) and half the original wind stress (red line) are also plotted.

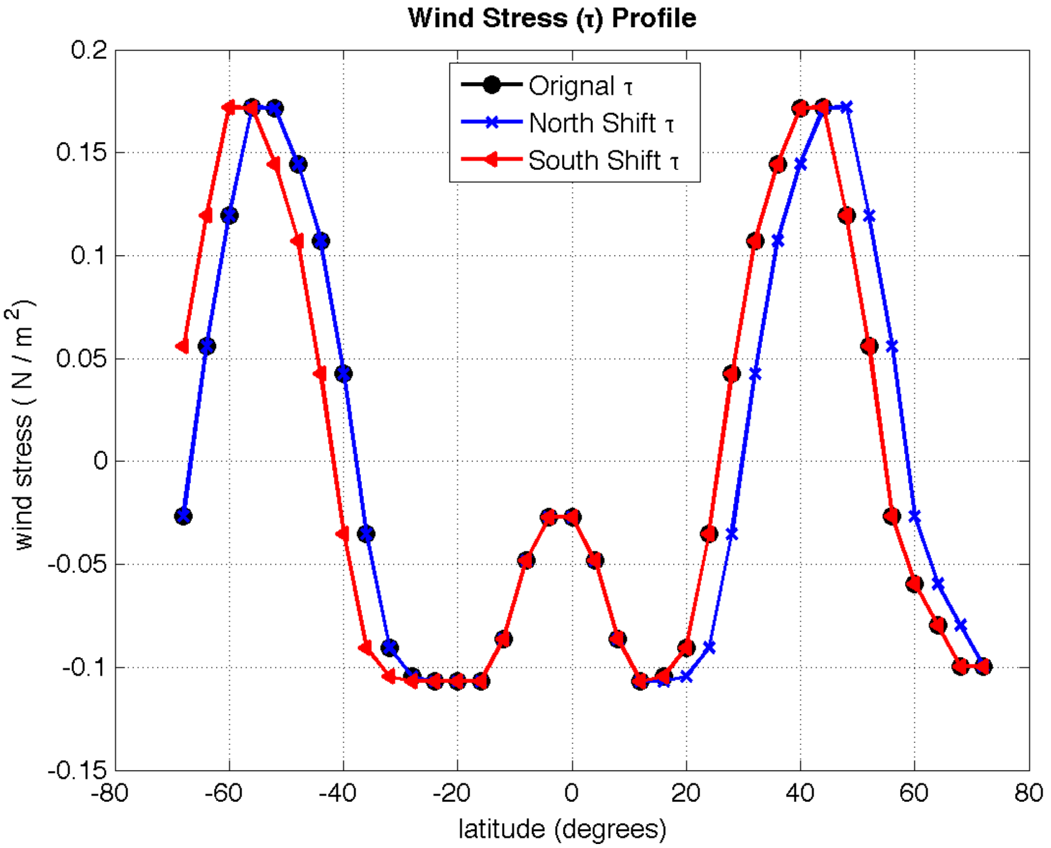

Figure 14: Wind stress profile for varying maximums. The wind stress profiles applied to the model (markers are plotted at each actual grid point). The original wind stress profile is plotted in black while original wind stress line shifted north (blue line) and the wind stress profile shifted south (red line) are also plotted.

(a) Bryan- Lewis Mixing (1979): Paper Exact

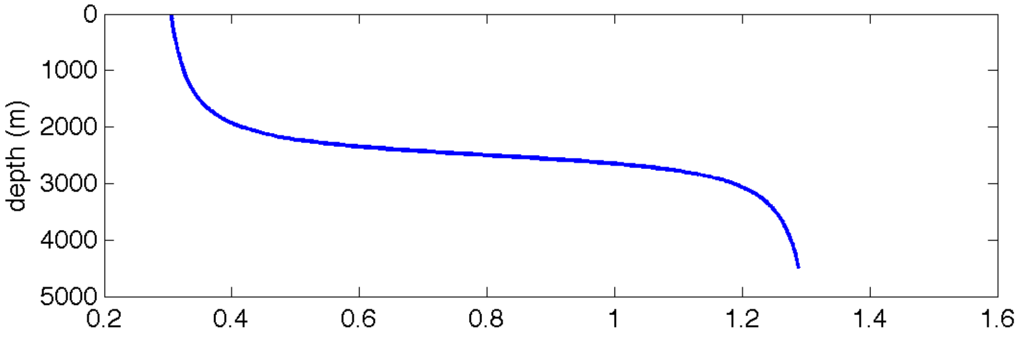

(b) Bryan- Lewis Mixing (1979): Approximation

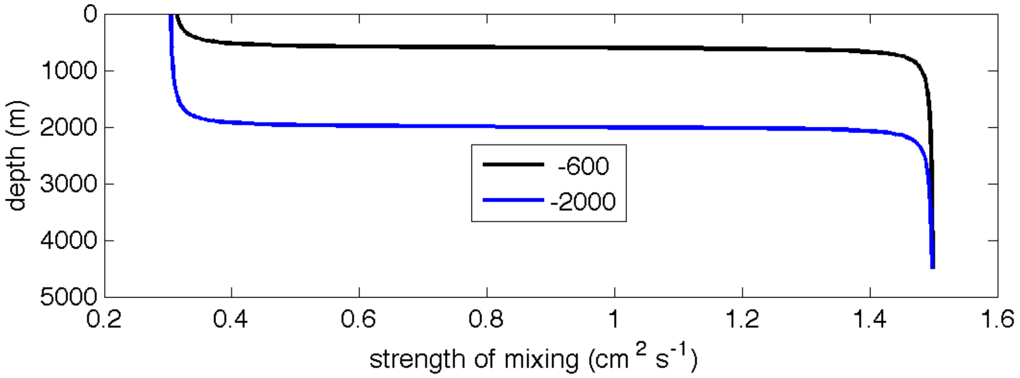

Figure 15: Bryan- Lewis mixing scheme profiles. A composite of the original Bryan-Lewis mixing scheme (Bryan and Lewis, 1979), panel (a), and a modified set of profiles, panel (b). In panel (b), the legend indicates different depths that the transition from surface to deep-water mixing values occurred.

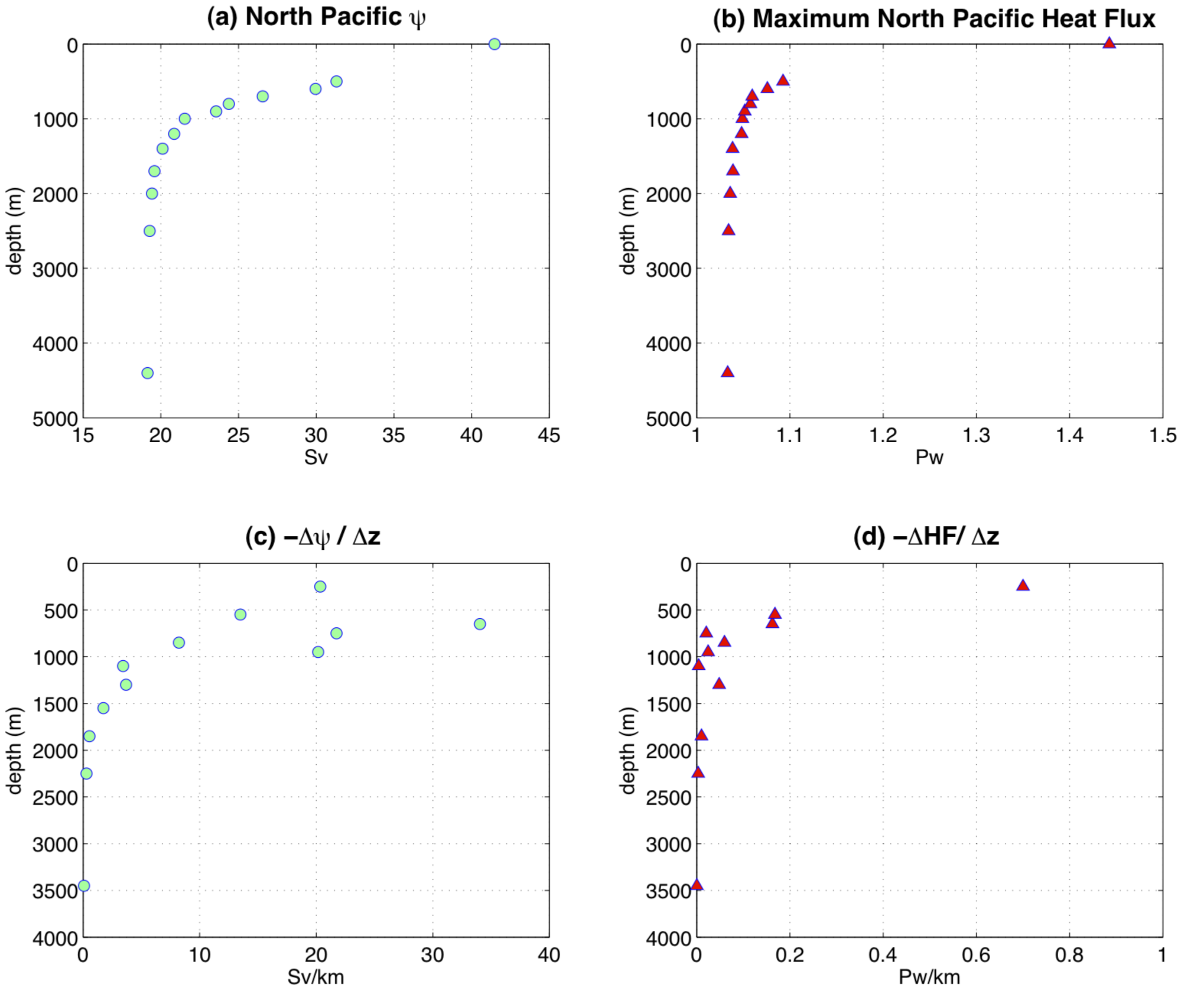

(a) North Pacific ψ

(b) Maximum North Pacific Heat Flux

(c) −Δψ / Δz

(d) −ΔHF/ Δz

Figure 16: MOC summary for Bryan- Lewis mixing scheme. (a) Maximum ψ in the North Pacific from simulations in which κ was increased from 0.3 to 1.5 $cm^2 s^{-1}$ at and below the depth shown on the y- axis. (b) Peak North Pacific heat flux given by increasing κ from 0.3 to 1.5 $cm^2 s^{-1}$ at and below the depth shown on the y- axis. (c) Finite- difference derivative of results in (a) with depth. (d) Finite- difference derivatives of results in (b) with depth.

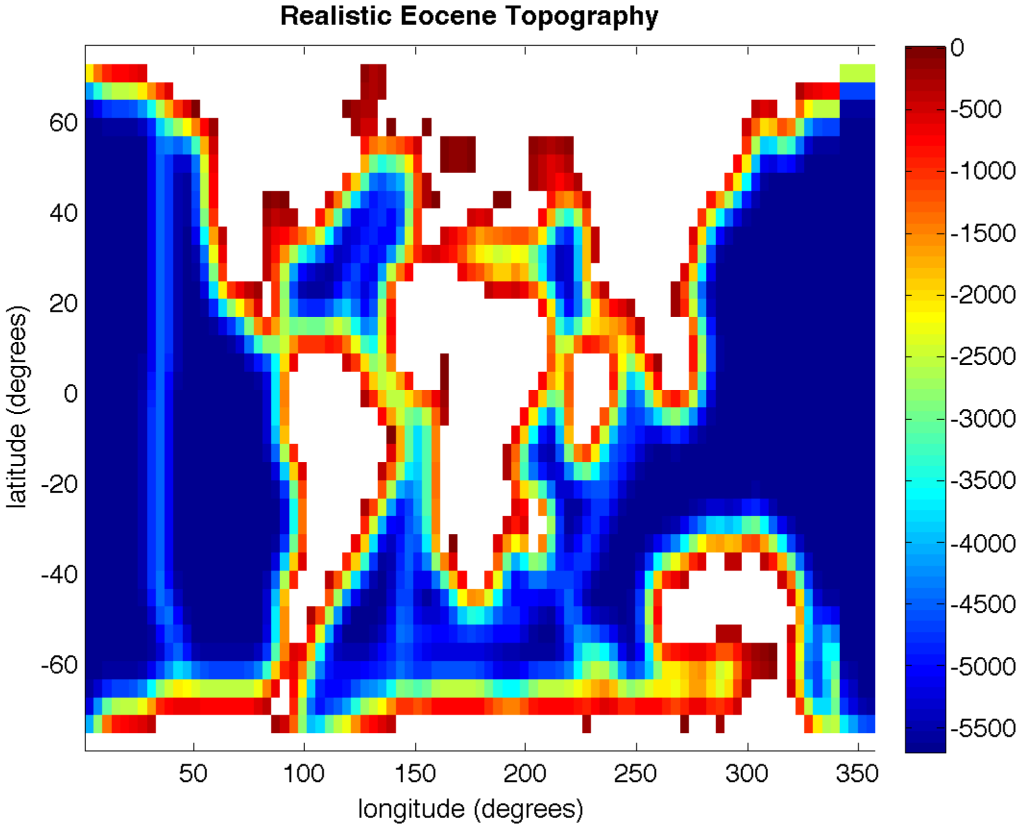

Figure 17: Realistic bathymetry for the early Eocene epoch. The map highlights a smaller Atlantic Ocean with a bigger Pacific Ocean, the Central American Seaway and a passageway through the Tethys Sea. White indicates land, while dark blue indicates deep ocean.

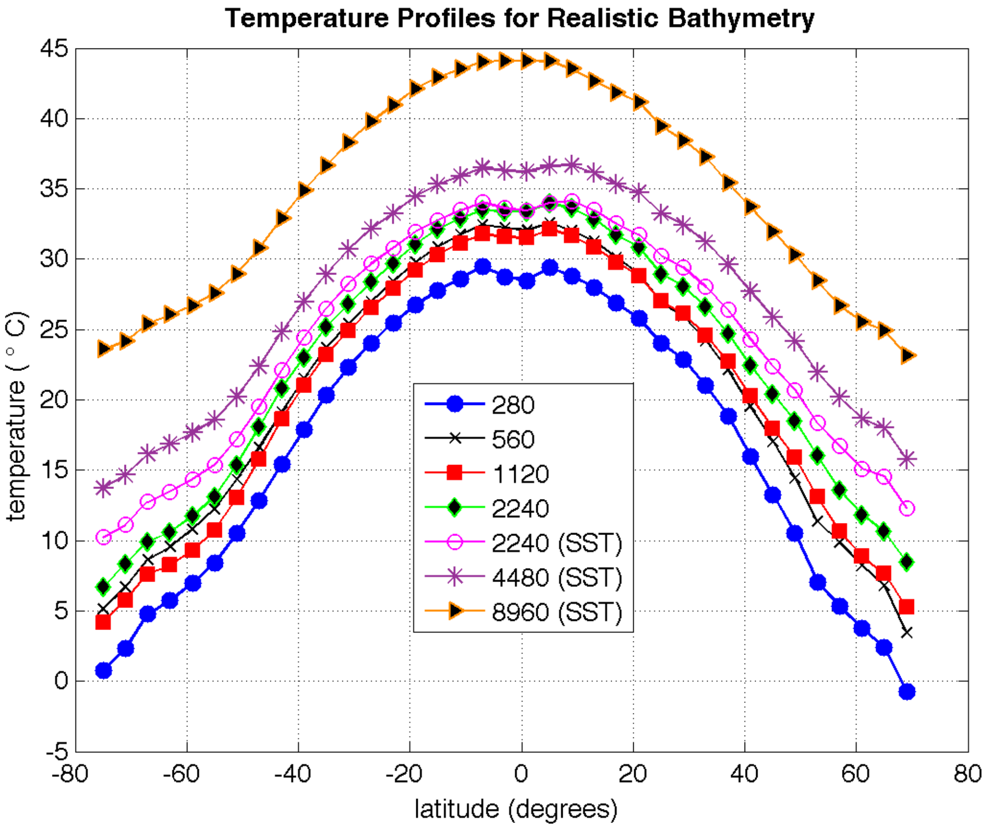

Figure 18: The zonal mean temperature profile for the Eocene bathymetry. Temperature profile to which the surface temperature field is restored (points are plotted at each actual grid point). The legend indicates the level of carbon dioxide with SST indicating model runs with a constant SST. The bathymetry used for this set of model runs can be found in Figure 17.

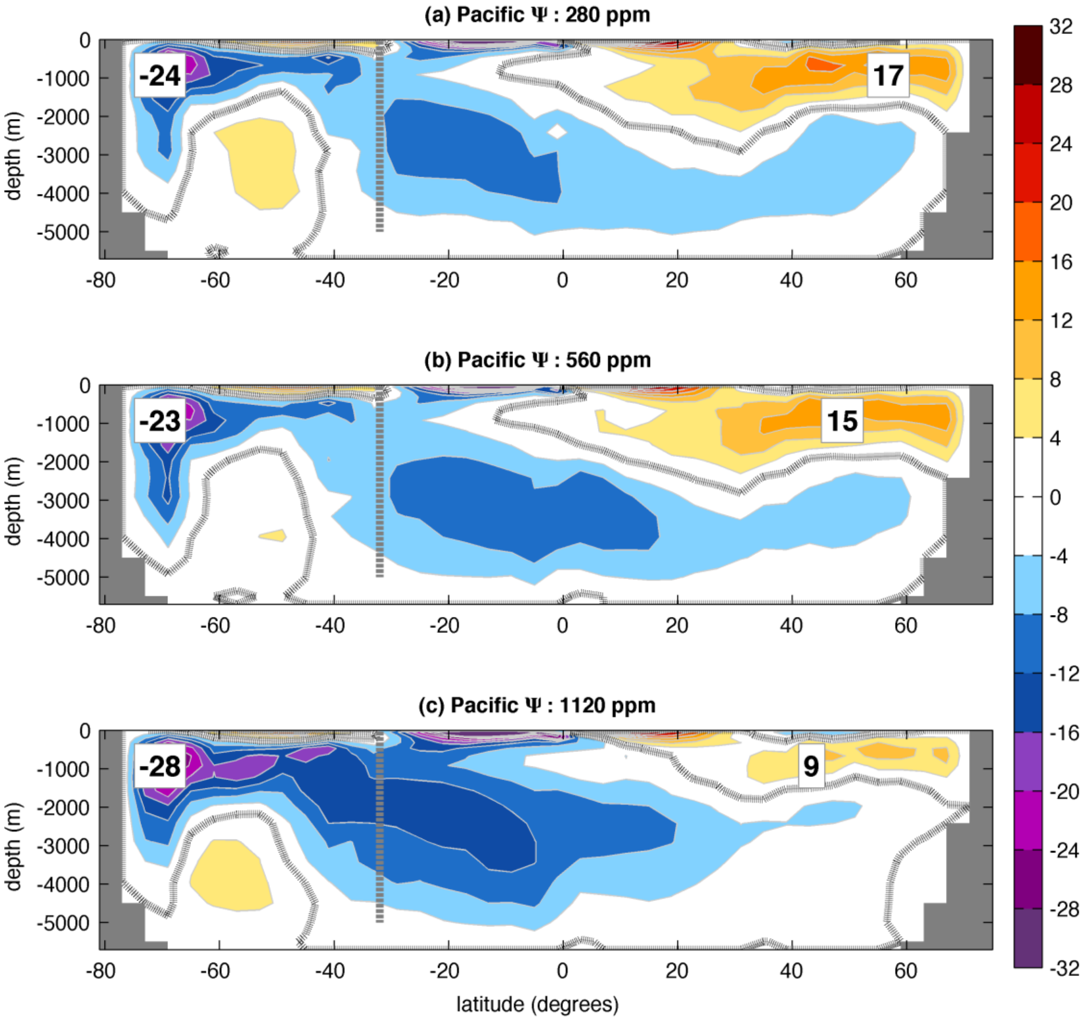

Figure 19: MOC in the Pacific Ocean with Eocene Bathymetry I. In all three panels, the maximum overturning in the Pacific Ocean is plotted. (a) shows the overturning in the Pacific for a CO_2 level of 280 ppm, (b) for 560 ppm, (c) for 1120 ppm. South of 39˚S the MOC is averaged globally. All of these cases are using boundary conditions taken from runs coupled to a slab ocean.

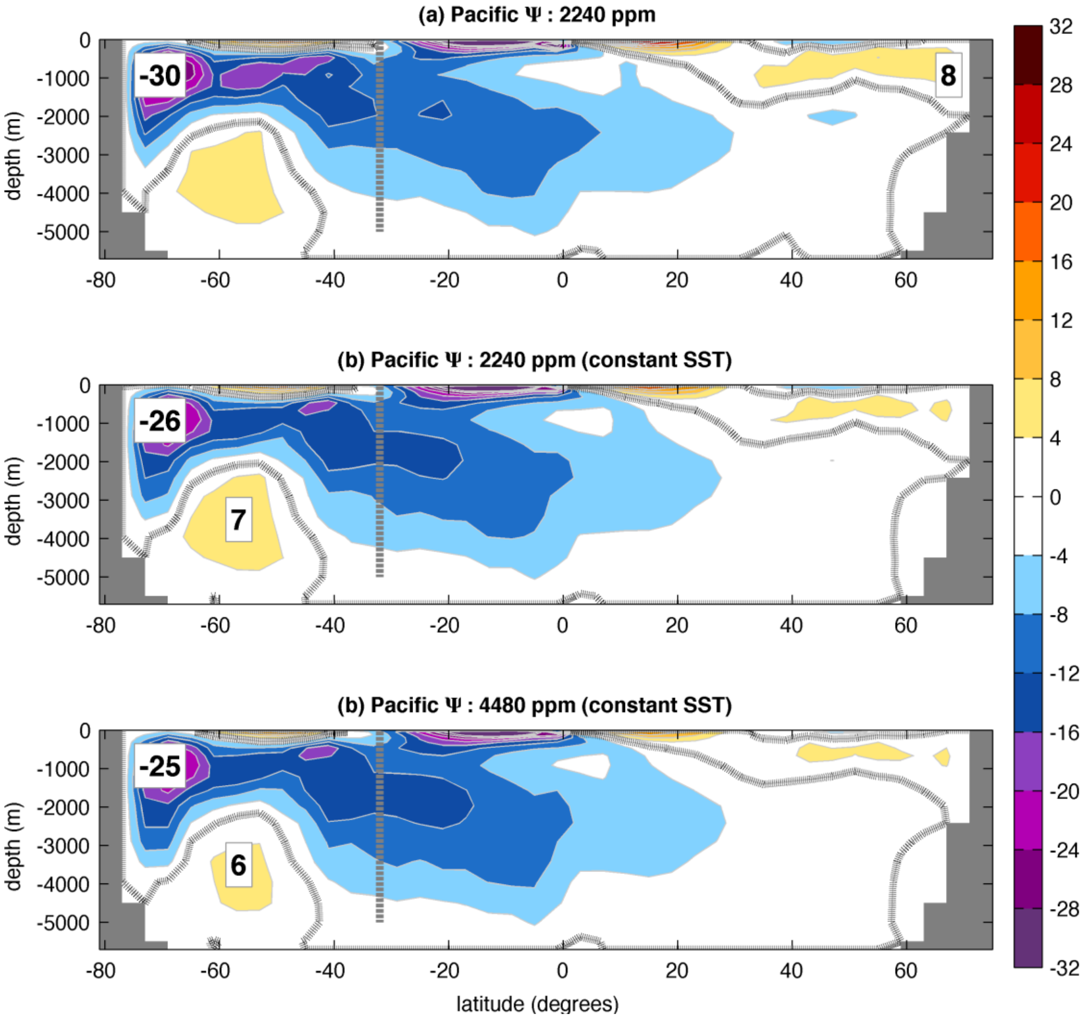

Figure 20: MOC in the Pacific Ocean with Eocene Bathymetry II. In all three panels the maximum overturning in the Pacific Ocean is plotted. (a) shows the overturning in the Pacific for a CO_2 level of 2240 ppm, (b) for 2240 ppm (constant SST), (c) for 4480 ppm (constant SST). South of 39˚S the MOC is averaged globally. (a) is using boundary conditions taken from runs coupled to a slab ocean, while (b) and (c) are using boundary conditions taken from runs with constant SST.

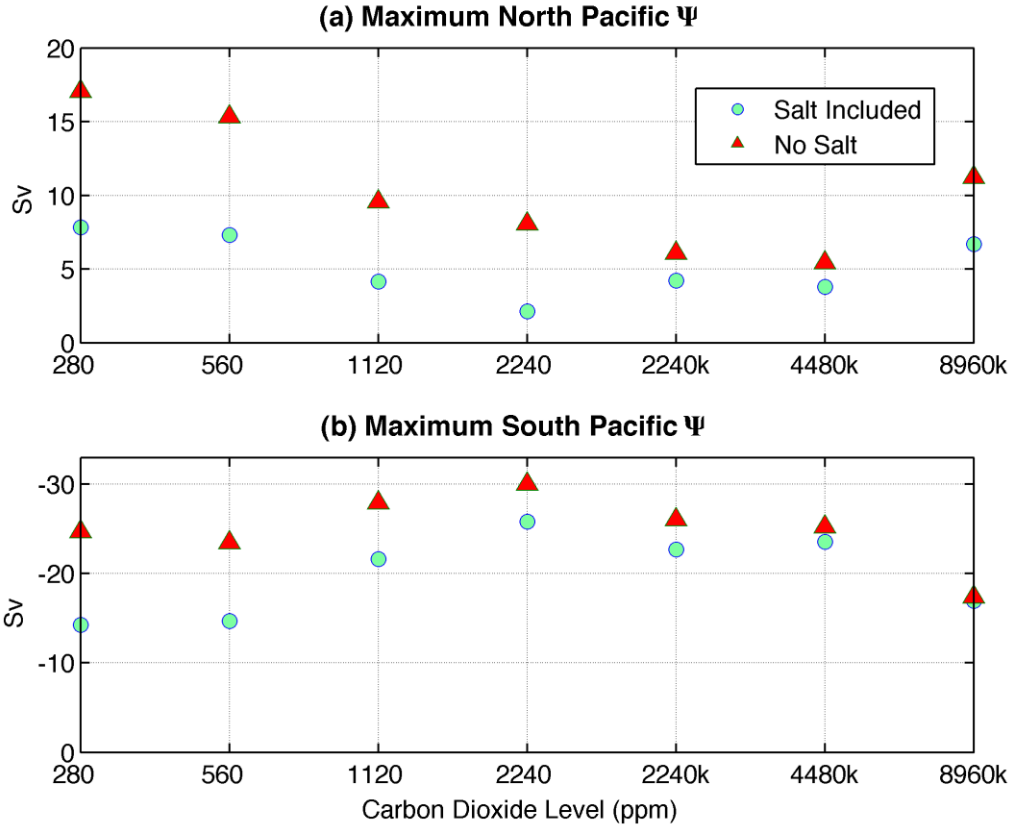

Figure 21: MOC summary including salinity. (a) shows the maximum overturning in the North Pacific for various CO_2 levels; (b) shows the maximum rate of overturning for the Southern Ocean. The CO_2 levels with a k indicate the data was used from the CAM3 model with a constant ocean SST. The CO_2 cases without the k indicate that data was used from the model with a slab ocean.

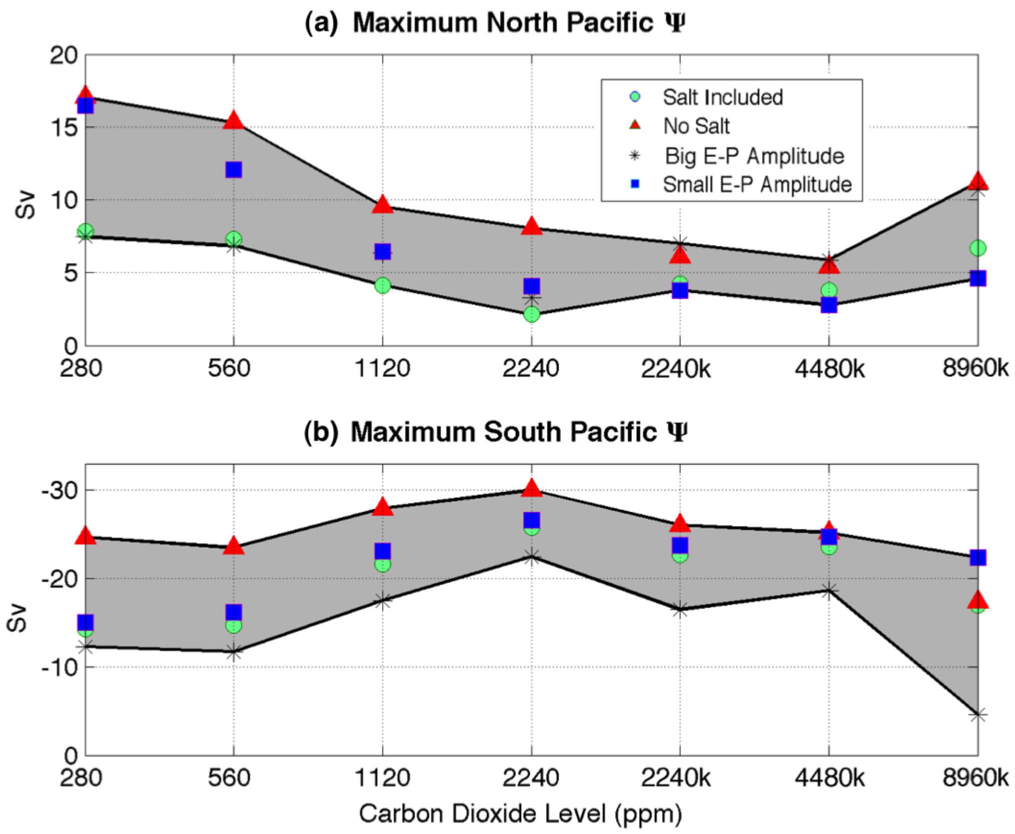

Figure 22: MOC summary of varying salinity. (a) shows the maximum overturning in the North Pacific for various CO_2 levels; (b) shows the maximum rate of overturning for the Southern Ocean. The CO_2 levels with a k indicate the data was used from the CAM3 model with a constant ocean SST. The CO_2 cases without the k indicate that data was used from the model with a slab ocean. The grey shaded region is the range of MOC values.

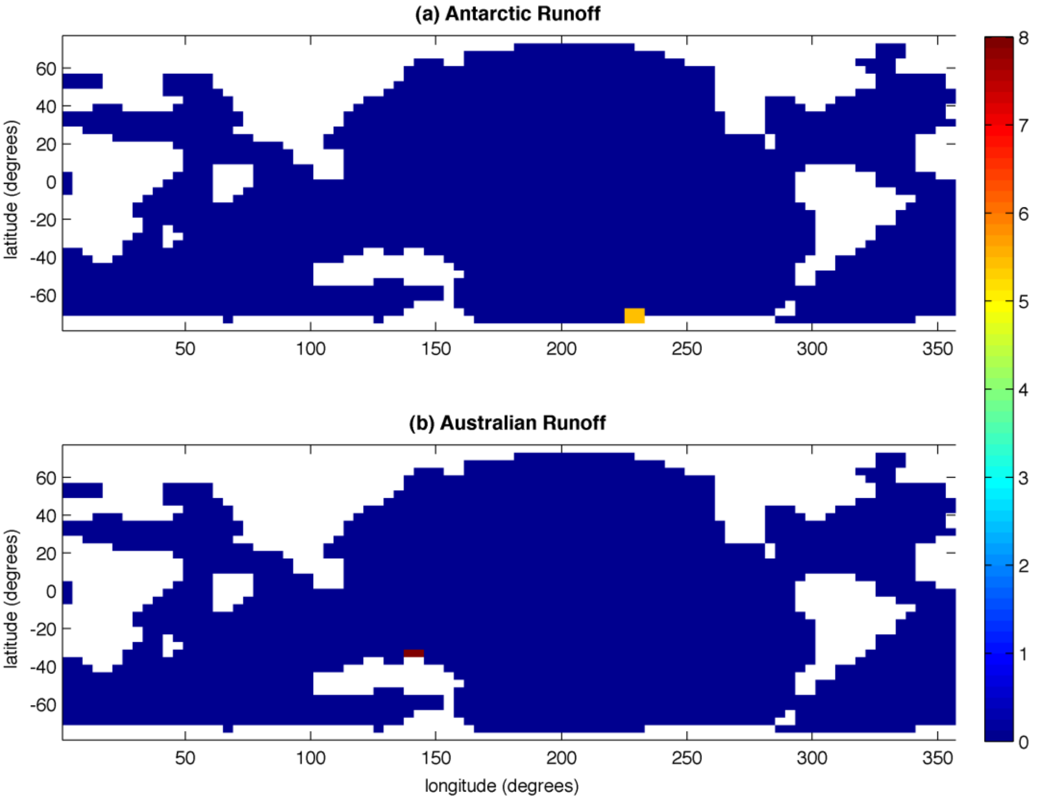

Figure 23: Overview of runoff simulations. (a) Runoff simulation in which river is coming off the coast of Antarctica. (b) Runoff simulation in which river is coming off the coast of Australia. The discharge rate is 16,200 m^3 s^{-1}.

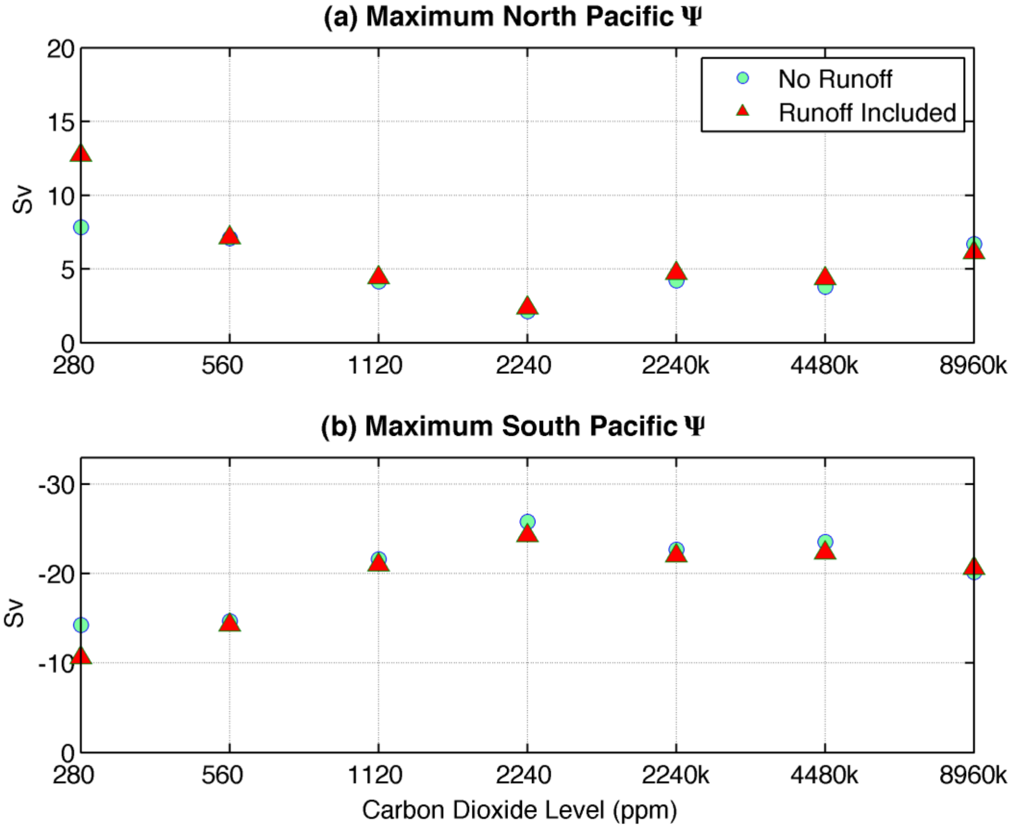

Figure 24: MOC summary for initial runoff. Panel (a) shows the maximum overturning (Sv) in the North Pacific for various CO_2 levels; Panel (b) shows the maximum rate of overturning for the Southern Ocean. The CO_2 levels with a k indicate the data was used from the CAM3 model with a constant ocean SST. The CO_2 cases without the k indicate that data was used from the model with a slab ocean.

(a) Zonal Average Density Gradient: 280 ppm

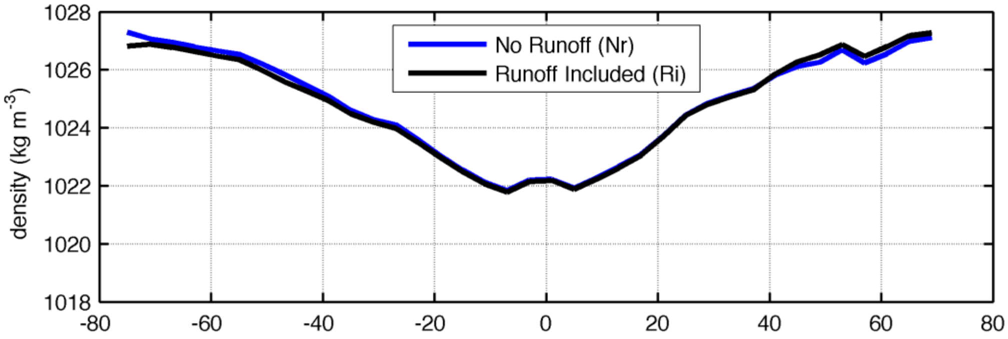

(b) Zonal Average Density Gradient: 2240k ppm

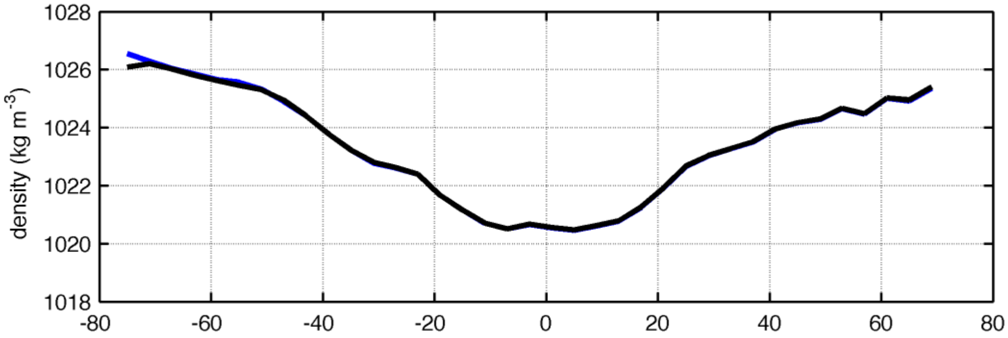

(c) Zonal Average Density Gradient: 4480k ppm

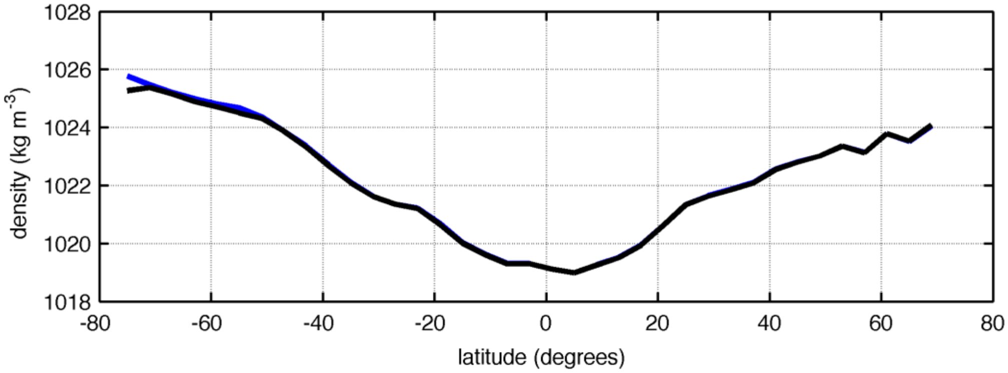

Figure 25: Density profile variability with runoff. Panel (a) shows the density gradients, averaged over all longitudes, for the E0 case. Panel (b) shows the density gradients for the E3k constant SST case. Panel (c) illustrates the density gradients for the E4k constant SST case.

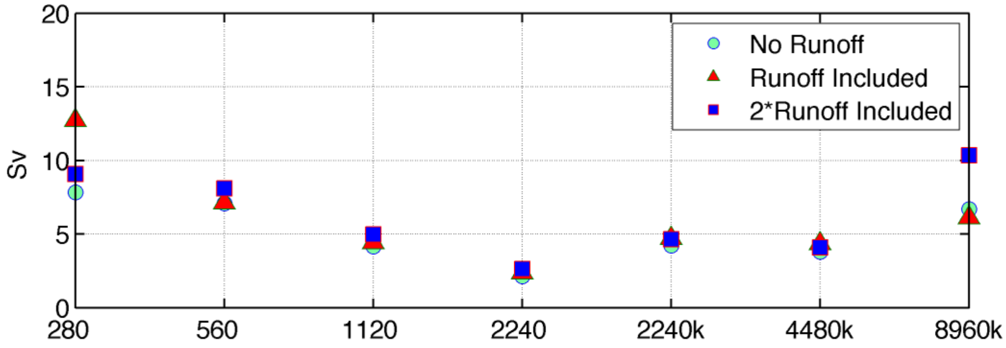
(a) Maximum North Pacific Ψ

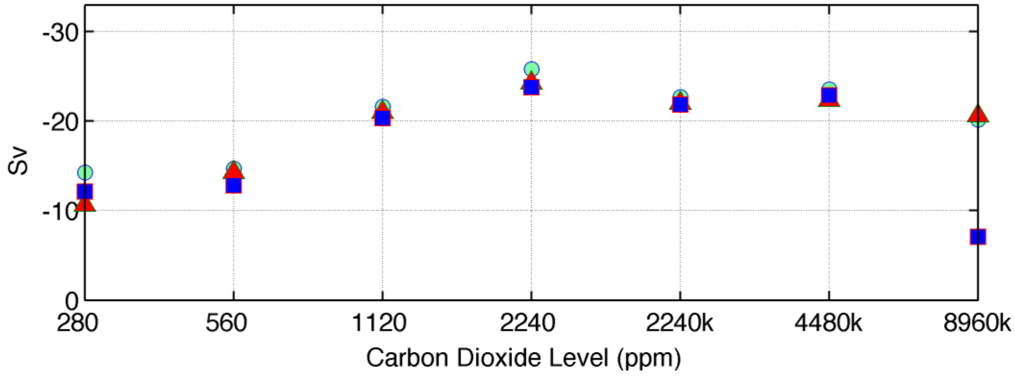
(b) Maximum South Pacific Ψ

Figure 26: MOC summary for double runoff. Panel (a) shows the maximum rate of overturning in the North Pacific for cases of increasing CO_2. Panel (b) shows the maximum rate of overturning in the South Pacific

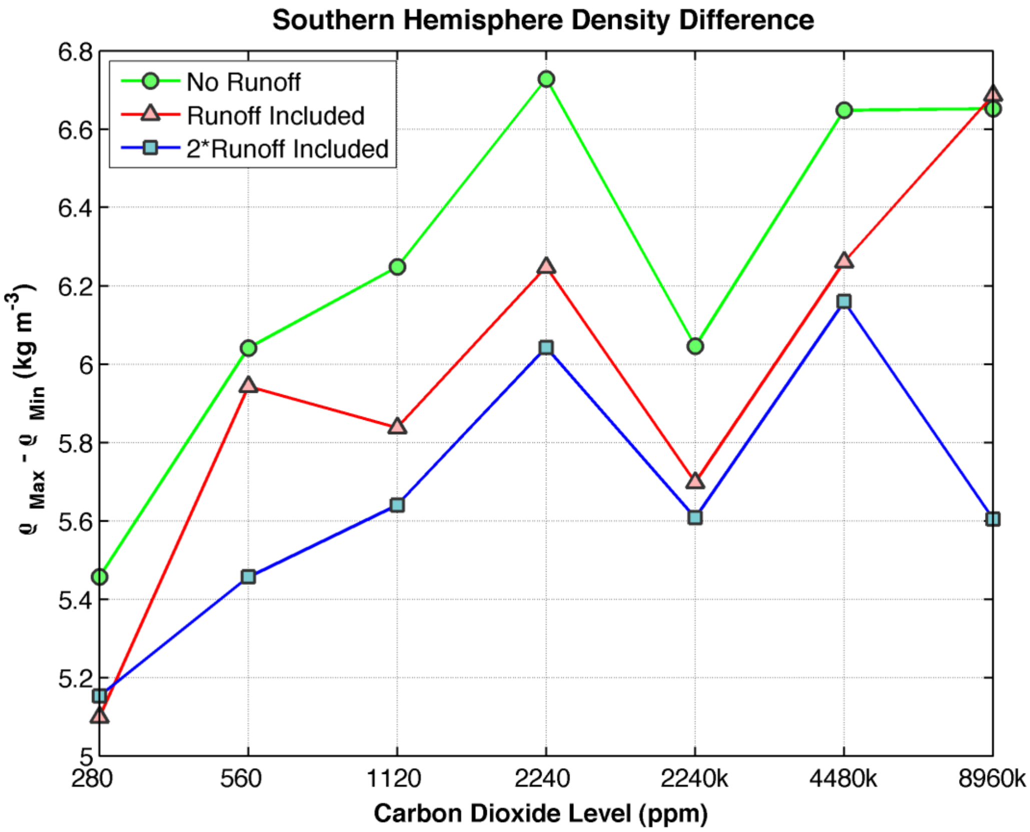

Figure 27: Southern Hemisphere density difference for varying runoff. The change in the magnitude of the density gradient, maximum minus minimum density in the Southern Hemisphere, with increasing CO_2.

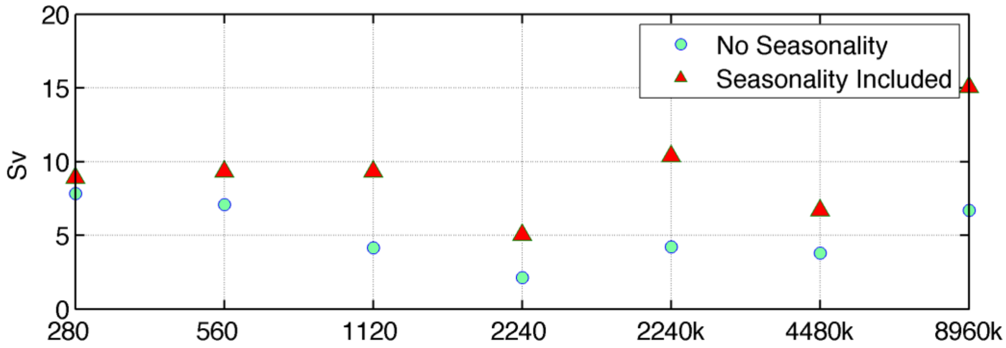

(a) Maximum North Pacific Ψ

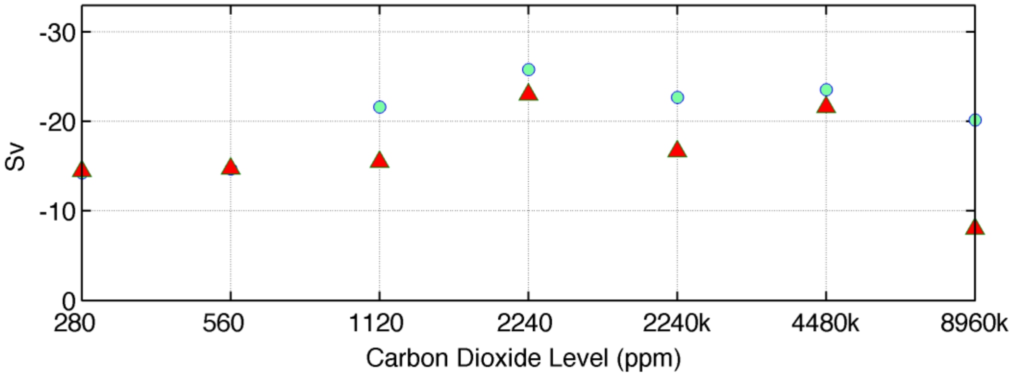

(b) Maximum South Pacific Ψ

Figure 28: MOC summary for seasonality. The rate of overturning in the North Pacific (a) and the South Pacific (b) for increasing levels of CO_2 in which seasonality was and was not included.

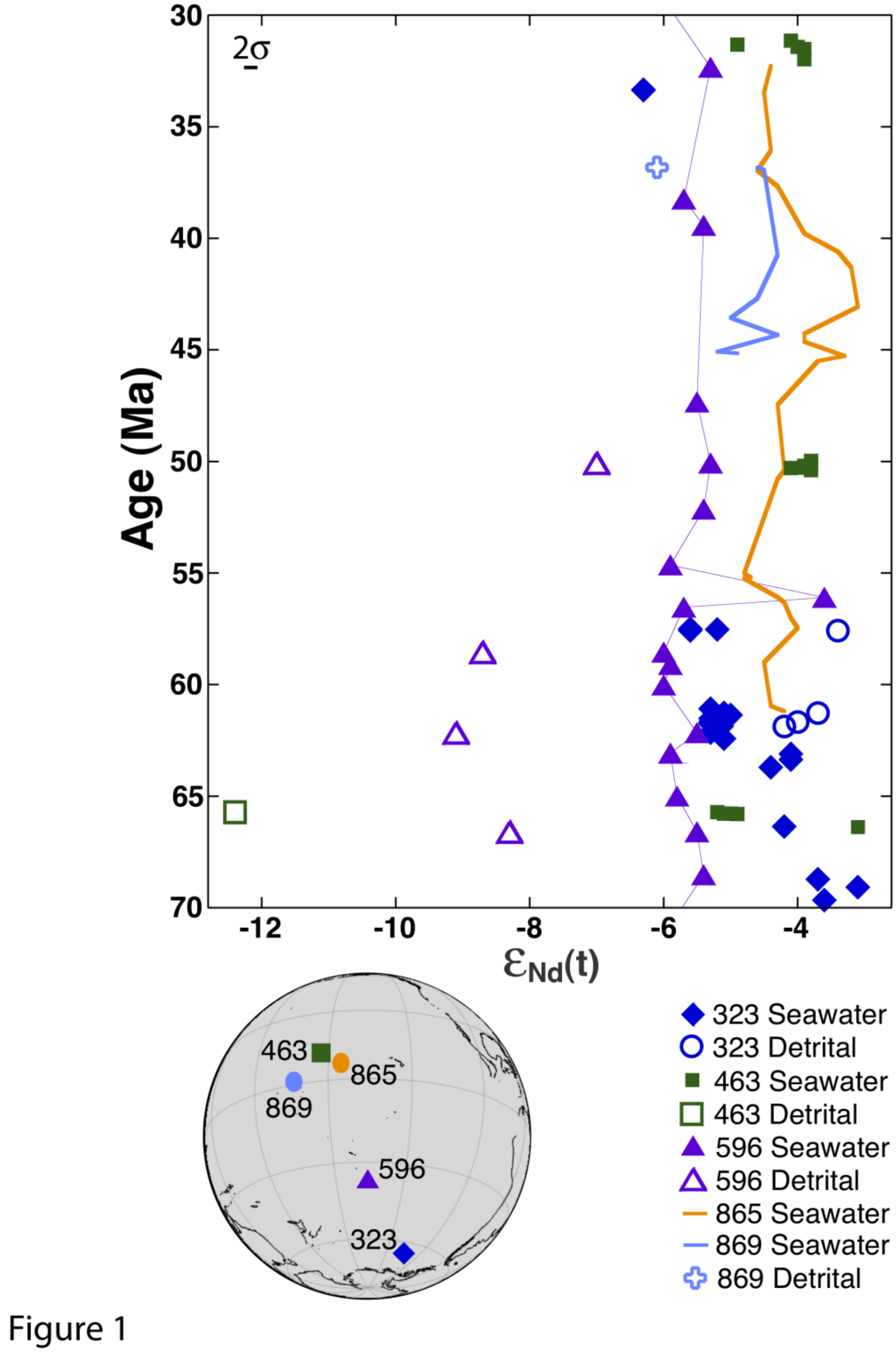

Figure 29: Derived ε_{Nd}(t) values from various DSDP and ODP sites. From Thomas et al., 2012.

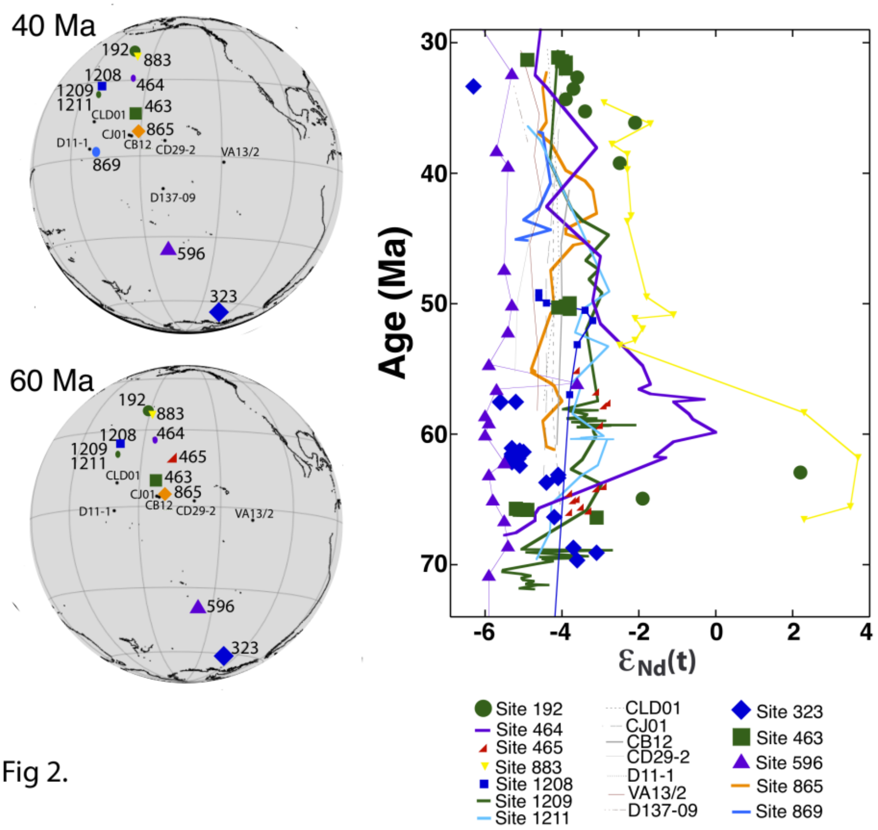

Fig 2.

Figure 30: Derived $\varepsilon_{Nd}(t)$ values from various DSDP and ODP sites. From Hague et al., 2012.

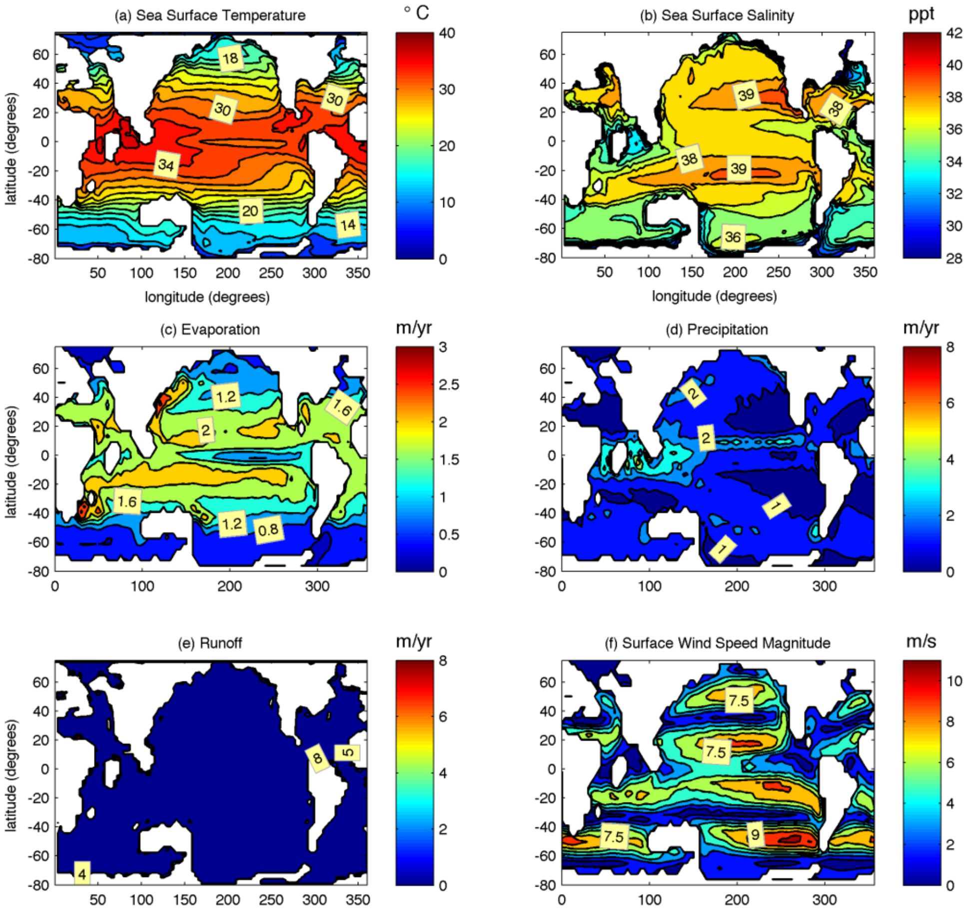

Figure 31: Various annual mean surface fields for 2240 ppm.

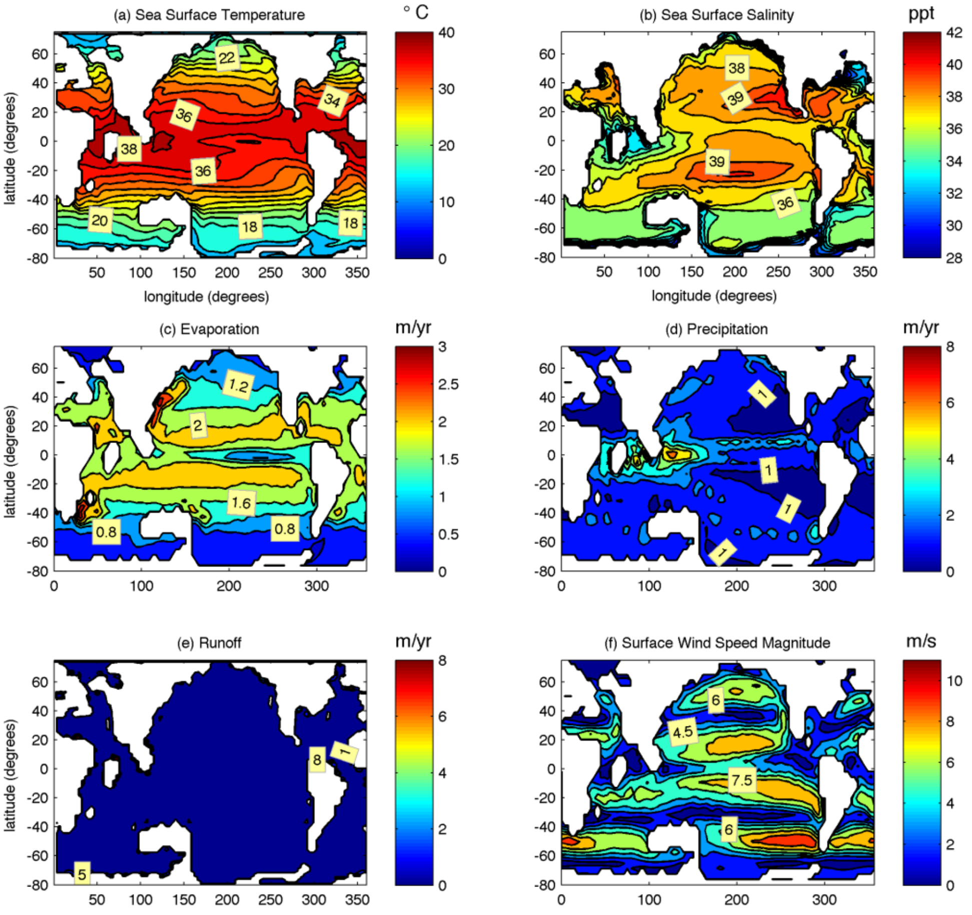

Figure 32: Various annual mean surface fields for 4480 ppm.

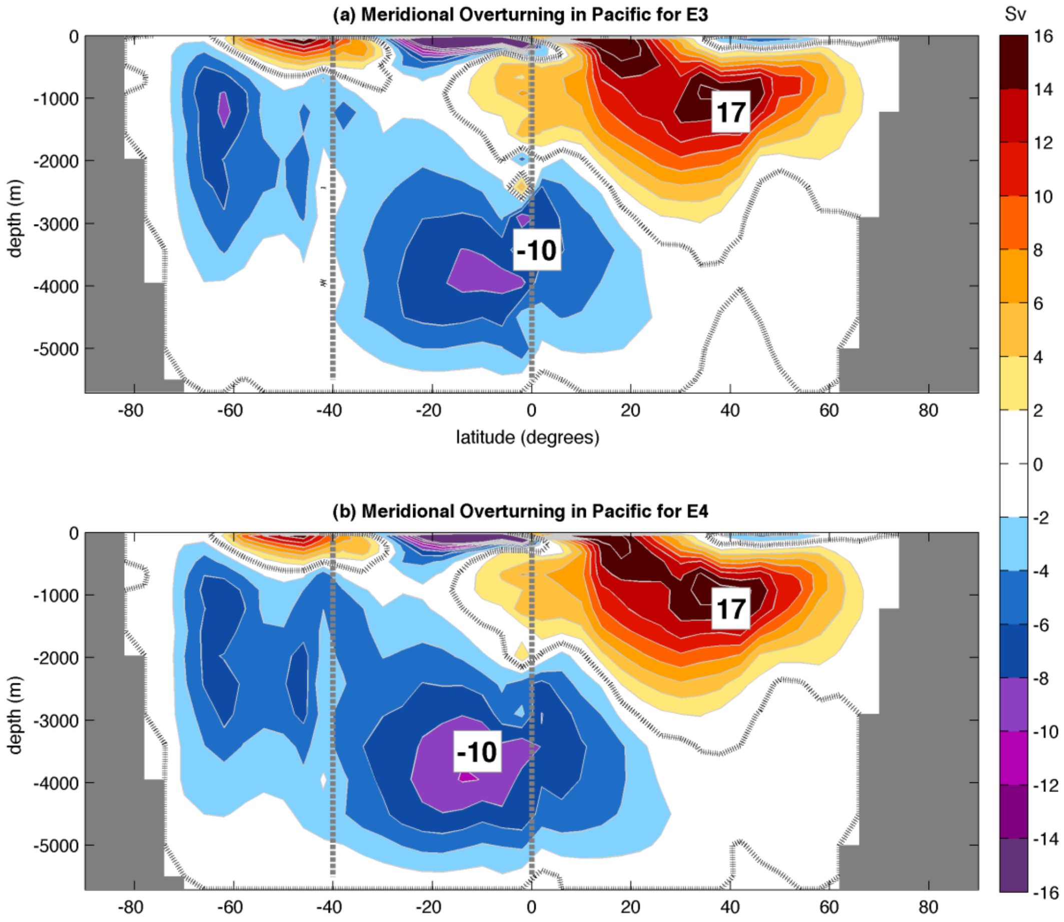

Figure 33: MOC summary for fully coupled simulations. The MOC in the Pacific basin for (a) E3 and (b) E4. In between the two dashed lines the circulation is averaged from the African coast across the Pacific Ocean to the South American coast.

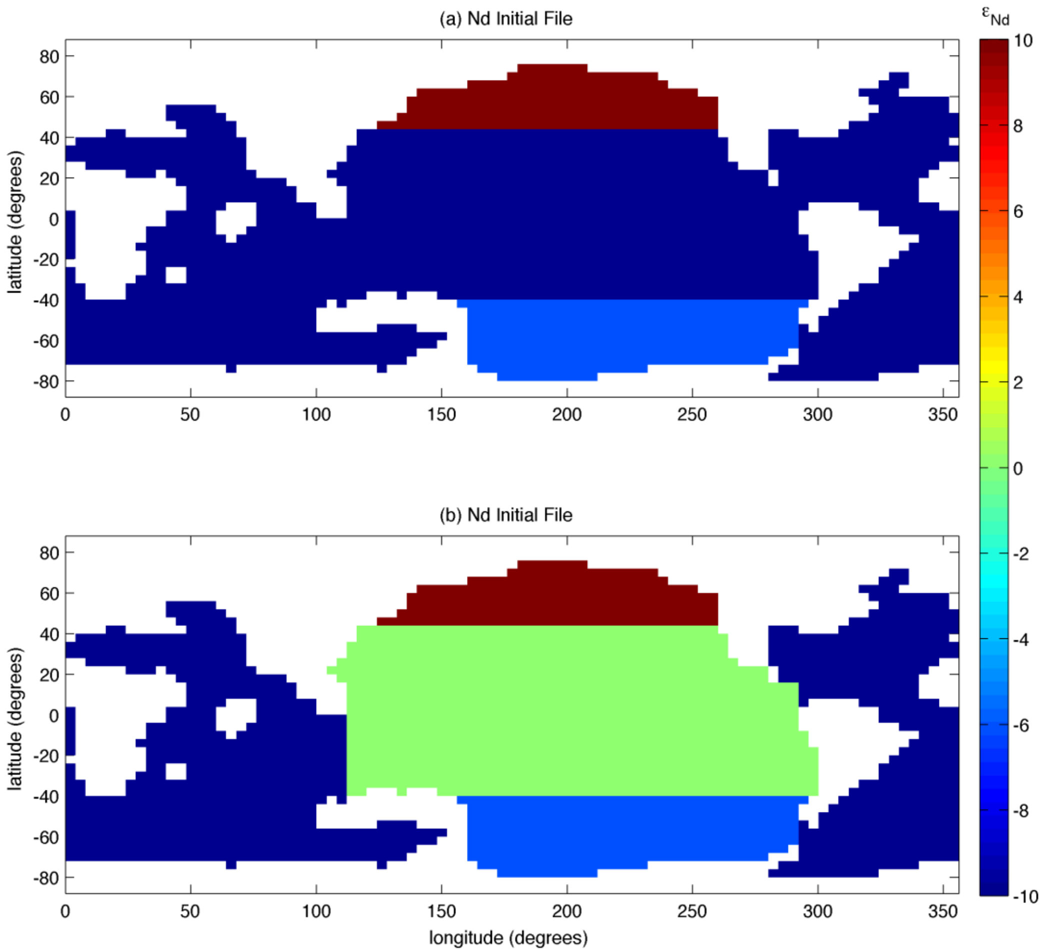

Figure 34: Initial Nd tracer distribution map in units of ε_{Nd}. Map 1 (a) has a North Pacific ε_{Nd} value of +10 and a South Pacific value of -6. Everywhere in the central Pacific ocean the value is 0, with all other locations having a value of -10. Map 2 (b) is similar to (a) except now the central Pacific has a ε_{Nd} value of -10 along with all the other locations.

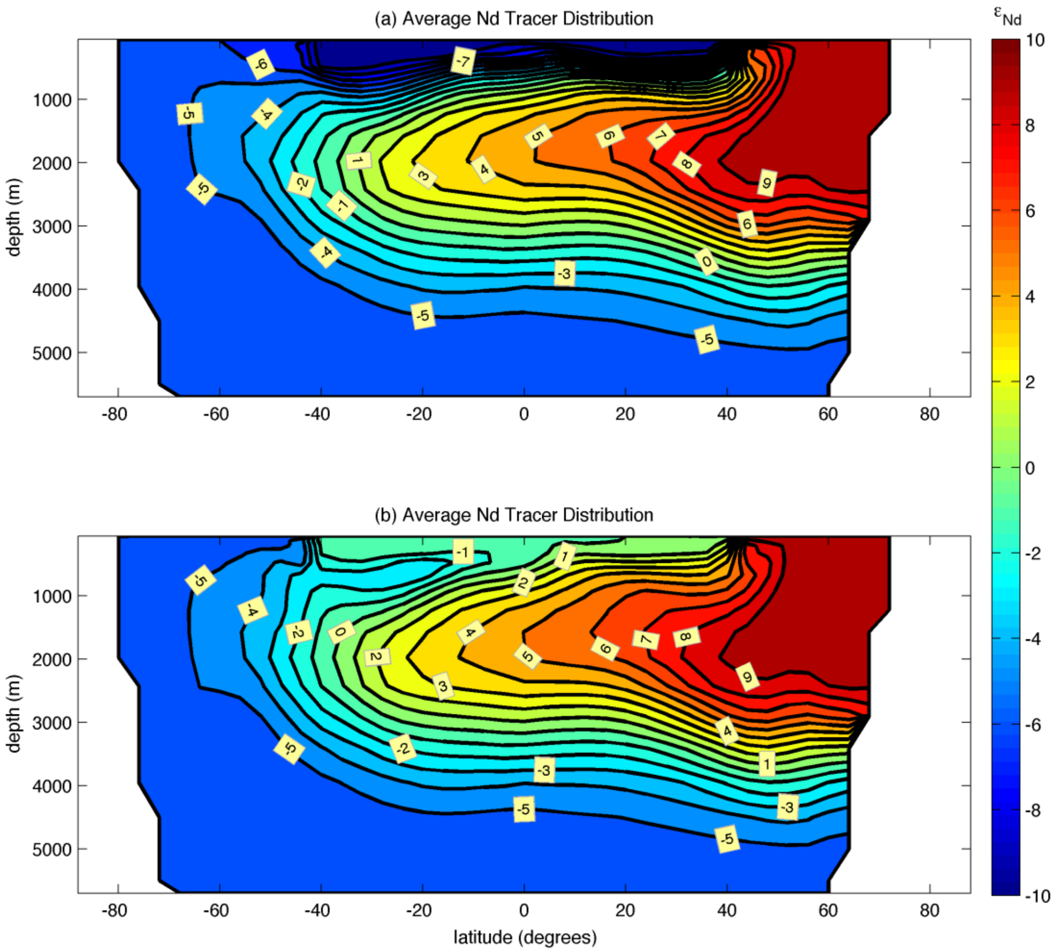

Figure 35: Nd tracer distribution averaged from 152°W to 148°E for E3. The initial file in Fig. 34a was used in (a) and the initial file in Fig. 34b was used in (b).

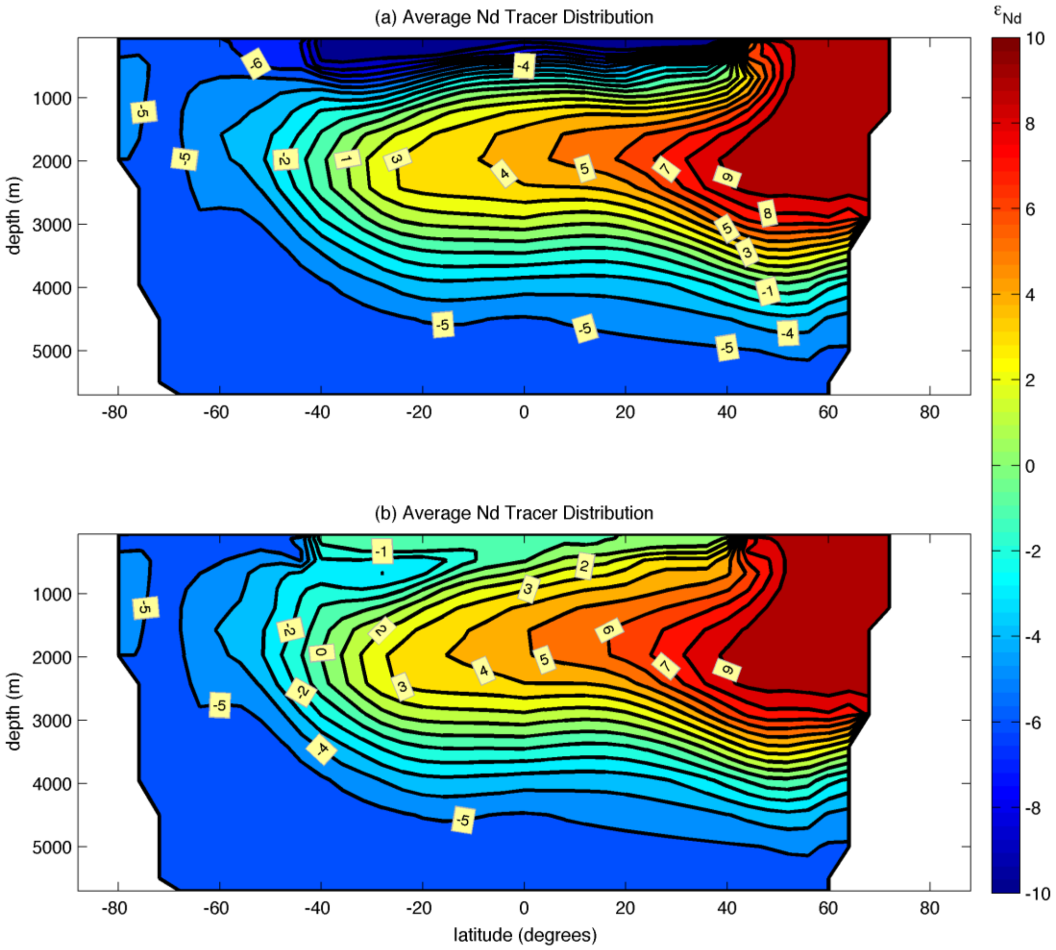

Figure 36: Nd tracer distribution averaged from 152°W to 148°E for E4. The initial file in Fig. 34a was used in (a) and the initial file in Fig. 34b was used in (b).

VITA

Name: Brian Andrew Haines

Address: Brian Haines
c/o Robert Korty
Department of Atmospheric Sciences
Texas A&M University
College Station, TX 77843-3150

Email Address: haines45@gmail.com

Education: B.S., Meteorology, Texas A&M University, 2010